AGU PUBLICATIONS

JGR

Journal of Geophysical Research: Atmospheres

RESEARCH ARTICLE
10.1002/2015JD023491

Key Points:
- Theoretical model predicting contrail particle properties at formation
- Conceptual framework for further contrail studies
- Soot emission reductions and threshold formation conditions reduce ice numbers

Correspondence to:
B. Kärcher,
bernd.kaercher@dlr.de

Citation:
Kärcher, B., U. Burkhardt, A. Bier, L. Bock, and I. J. Ford (2015), The microphysical pathway to contrail formation, *J. Geophys. Res. Atmos.*, *120*, 7893–7927, doi:10.1002/2015JD023491.

Received 9 APR 2015
Accepted 1 JUL 2015
Accepted article online 4 JUL 2015
Published online 13 AUG 2015

The microphysical pathway to contrail formation

B. Kärcher[1], U. Burkhardt[1], A. Bier[1], L. Bock[1], and I. J. Ford[2]

[1]Institut für Physik der Atmosphäre, DLR Oberpfaffenhofen, Wessling, Germany, [2]Department of Physics and Astronomy, University College London, London, UK

Abstract A conceptual framework to predict microphysical and optical properties of contrail particles within a wingspan behind the source aircraft is developed. Results from two decades of contrail observations and numerical simulations are reviewed forming the basis of theoretical model development. The model utilizes cloud theory applied to the dynamics and thermodynamics of jet aircraft exhaust plumes in upper tropospheric conditions. Droplet nuclei include soot particles emitted from aircraft engines and atmospheric particles entrained into the plume. These precursor particles activate into copious homogeneously freezing water droplets as the plume relative humidity rises beyond liquid water saturation. A unimodal size spectrum of ice particles develops wherein ice particles grow to micrometer mean sizes. Contrail particle formation is analyzed over a wide range of soot emissions relating to conventional jet fuels as well as to alternative aviation fuels producing much less soot and volatile particle emissions. For current aviation fuels and propulsion technology, the number of contrail ice particles scales roughly in proportion to the number of emitted soot particles that act as water condensation nuclei despite their poor hygroscopicity. Close to the contrail formation threshold, only few plume particles can be water activated and freeze. Implications for effects of alternative fuels on contrails, an arena for future scientific exploration, are outlined.

1. Introduction

Jet aircraft contrails occur primarily at high altitudes in the upper troposphere. They persist and spread in ice-supersaturated air as man-made cirrus clouds capable of exerting a substantial global radiative forcing, making contrail cirrus the largest aviation climate forcing agent [*Burkhardt and Kärcher*, 2011], with a large but poorly explored potential for reducing the aviation climate impact. Mitigating the climatic effects of contrails not only requires a robust understanding of how atmosphere and climate react in response to contrail cirrus but also of how contrails form in the first place.

A thermodynamic model is available predicting the physical formation conditions of jet exhaust contrails as a function of atmospheric temperature, pressure, and humidity, as well as characteristics of the fuel combustion process and the contrail-producing aircraft engines [*Schmidt*, 1941; *Appleman*, 1953; *Schumann*, 1996]. It has been employed in large-scale models to parameterize the occurrence of contrails [*Ponater et al.*, 2002] and the ice-supersaturated areas supporting persistent contrails [*Burkhardt et al.*, 2008]. The temperatures for the onset of contrail formation predicted by thermodynamics (henceforth threshold temperatures) have been confirmed by in situ measurements.

The thermodynamic approach rests on the empirical assumption that, while hot and moist exhaust plumes mix with colder and drier atmospheric air, contrails form once the gas mixture surpasses water-saturated conditions, supporting the formation and growth of water droplets. At the low temperatures where contrails mostly form, supercooled water droplets freeze very rapidly, as the associated homogeneous ice nucleation process is the dominant freezing mode. Contrails become visible as line-shaped clouds already at formation directly behind the aircraft engines, despite their small geometrical thicknesses, suggesting that they contain many ice particles [*Kärcher et al.*, 1996]. Observations have shown that young contrails are composed of a much higher number of smaller ice particles than natural cirrus clouds [*Heymsfield et al.*, 2010].

Equilibrium thermodynamics predicts whether contrails form or not but gives no clue about the underlying formation mechanisms and the physical properties of the contrail particles, leaving, for instance, the total ice particle number density and mean ice particle size undetermined. However, those variables must be simulated with confidence in models in order to predict the evolution and radiative response of contrails.

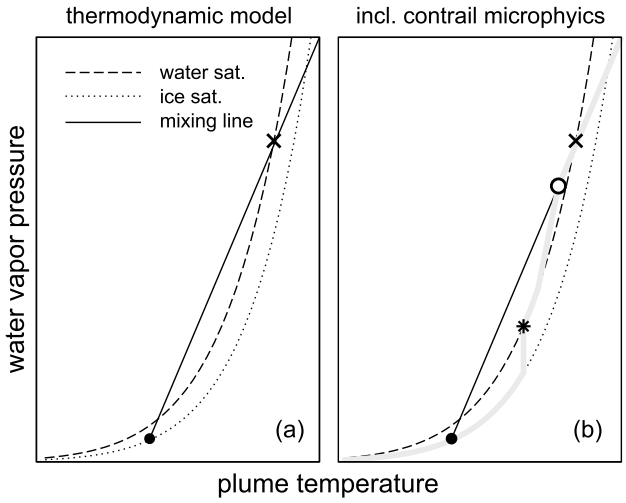

Figure 1. Schematic of supercooled water and ice saturation vapor pressures and average mixing line of a cooling jet aircraft exhaust plume (a) without and (b) with contrail microphysics as a function of plume temperature. The plume age increases as the plume temperature decreases to its atmospheric value corresponding to ice saturation (filled circle). The cross marks first water-saturated conditions in the plume. The open circle marks the point at which contrail water droplets that have already formed start to deplete significantly water vapor above water saturation (activation-relaxation). The star marks the point at which frozen droplets start to quench ice supersaturation (freezing-relaxation). The separation between these two points is exaggerated for clarity. The exact location and rate at which relaxation occurs in each phase transition depend contrail particle properties. Our theory tracks the evolution of plume relative humidity and provides physically based estimates of contrail particle properties at the point of their formation.

Sophisticated computer models have been developed simulating the physical and chemical processes governing contrail formation [*Brown et al.*, 1997; *Yu and Turco*, 1998; *Kärcher*, 1998a; *Wong and Miake-Lye*, 2010]. Those parcel models include turbulent mixing as the key dynamical factor responsible for the generation of supersaturated conditions conducive to ice formation within young jet aircraft exhaust plumes.

Here we devise a theory describing the nonequilibrium, microphysical pathway to contrail formation, extending the thermodynamic approach. By considering the dynamical evolution of jet plumes and the microphysics of plume particles, we obtain physically based relationships predicting number and size of contrail particles and other contrail properties in the jet regime [*Kärcher and Fabian*, 1994] of aircraft wake development. The observation-based theoretical framework discussed here might prove to be useful in guiding parameterization development regarding ice formation in contrails for application in global models, as well as interpreting results from complex numerical simulations and upcoming field measurements. By identifying the few most important processes and treating them analytically, our approach is capable of replicating results from more detailed numerical plume models, but at a much lower computational cost. Importantly, it provides deeper insights into underlying physical mechanisms, thereby increasing confidence in the ability to predict atmospheric effects of contrails, in particular regarding the mitigation of the climate impact of contrail cirrus. Processes related to the dynamics of aircraft wake vortices [*Miake-Lye et al.*, 1993; *Lewellen and Lewellen*, 2001; *Holzäpfel*, 2003; *Paugam et al.*, 2010; *Unterstrasser and Sölch*, 2010] taking place at later stages corresponding to distances of many wingspans behind an airplane and potentially reducing the ice particle number are not the subject of our study. Moreover, we omit effects on ice formation of nanometer-sized volatile particles produced in nascent aircraft plumes. The possible use of sulfur-free alternative aviation fuels will reduce the ability of those particles to act as contrail nuclei expected to occur for strongly reduced soot emissions and low atmospheric temperatures.

In Figure 1, we sketch supercooled water and ice saturation (equilibrium) vapor pressures and a representative mixing line of a cooling jet exhaust plume (a) without and (b) including contrail microphysics. As suggested in Figure 1a, the plume air gradually dilutes and cools by isobaric mixing with surrounding air. During mixing, supersaturation — a physical condition necessary to form and grow water-containing particles — occurs once the mixing line first crosses the saturation vapor pressure curves. The mixing line determines the bulk evolution of the partial pressure of water vapor, averaged over the whole plume cross section, in the absence of condensation. Its slope depends on air pressure and aircraft- and fuel-related parameters. As time progresses, the mixing line approaches atmospheric conditions (dot) controlling contrail persistence. Figure 1b illustrates the evolution of the water vapor pressure including effects of contrail particle formation (gray curve). The cross signifies conditions at which the plume first becomes supersaturated with respect to the liquid water phase, so that aerosol particles activate into water droplets which start to quench the supersaturation by condensation ("activation-relaxation," circle). The star marks the transition region at which ice particles cause the water vapor partial pressure to relax further toward ice saturation ("freezing-relaxation"). Activation-relaxation and

freezing-relaxation are only a few degrees (a few tenths of a second) apart in terms of plume temperature (plume age).

Much of what we know about young contrails derives from basic thermodynamic principles (section 2) and from in situ or remote sensing observations and numerical simulations (section 3). To develop a comprehensive understanding of contrail formation, cloud physical theory should be taken into consideration. Capturing the main processes and interactions controlling contrail formation is a great challenge of our theory-based approach (section 4). Besides arriving at a description that may prove to be useful to parameterize the physical processes responsible for contrail ice formation, we gain deeper insight into the microphysical pathway to contrail formation (section 5). This is important in order to study effects of changing emission parameters on the microphysical and optical properties of contrails. Our work concludes with a summary of main results and highlights implications regarding effects of alternative aviation fuels on contrail properties (section 6).

2. Thermodynamics of Aircraft Exhaust Plumes

We summarize key features of the thermodynamic approach to predict contrail occurrence and study for the first time physical plume conditions controlling water phase transitions during jet contrail formation.

2.1. Crucial Constraints for Contrail Formation

Contrails form in nascent exhaust plumes of cruising aircraft by activating copious supercooled water droplets which freeze into ice particles. Since atmospheric relative humidities (RH) at cruising altitudes are too low to support the persistence of liquid water droplets but frequently allows ice-phase particles to exist [*Gettelman et al.*, 2006; *Lamquin et al.*, 2012], freezing must take place in the moist exhaust plume very soon after droplet formation in order to produce persistent contrails.

A requirement for contrail formation, postulated by *Appleman* [1953], implies that abundant plume aerosol particles act as water condensation centers ("water-saturation constraint"). An approximate lower visibility limit in terms of the nucleated ice particle number in contrails at formation ("visibility constraint") has been estimated to be 10^4 cm^{-3} at a plume age of 0.3s for a small-scale research aircraft [*Kärcher et al.*, 1996]. In addition, lower limit estimates for the ice water content, 4 (10) mgm^{-3}, have been reported for faint (persistent) contrails [*Appleman*, 1953], but it is not clear for which contrail ages those values are representative because the contrail ice water content increases with time after formation.

If the water-saturation constraint was not necessary and supersaturation with respect to ice sufficient, threshold temperatures for the formation of visible contrails would be higher than observed [*Kärcher et al.*, 1998, Figure 3]. As a consequence, the vast majority of plume particles cannot be very efficient heterogeneous ice nuclei, i.e., particles that form ice well below water saturation. This said, in situ measurements do not rule out that few contrail ice particles might form upon suitable ice nuclei as long as the plume is ice supersaturated during mixing (in which case the mixing line in Figure 1a would be required to cross the ice saturation, but no longer the water saturation curve); should such contrails exist, they need to be optically very thin.

In the thermodynamic approach, the threshold temperature, Θ_G, is determined by tangential contact between the average mixing line and the water saturation vapor pressure curve (Figure 2a, thick solid line). Therefore, Θ_G is the highest atmospheric temperature for contrails to form in a water-saturated atmosphere (RH = 100%). Threshold temperatures for conditions with an atmospheric relative humidity RH $<$ 100%, denoted by Θ(RH), are lower. The lowest value of Θ corresponds to a completely dry atmosphere. The actual atmospheric temperature, T_a, and RH—marking the endpoint of the mixing line (Figure 1)—determine whether the plume will be supersaturated with respect to liquid water at some point during its evolution.

Therefore, the thermodynamic criterion for contrail formation can be expressed as $T_a \leq \Theta$(RH). In the thermodynamic theory, the factors affecting the threshold temperature can be encapsulated in a single parameter, the slope of the average mixing line [*Schumann*, 1996]:

$$G = \frac{c_p \mathcal{M}_w P}{0.622 Q(1-\eta)}, \tag{1}$$

where c_p is the isobaric specific heat of air, $\mathcal{M}_w$ is the mass emission index of water vapor, P is the air pressure, and η (overall propulsion efficiency) is the ratio of the work performed by the aircraft against the drag (balanced by the thrust) and the energy flow generated by combustion of jet fuel with a specific combustion

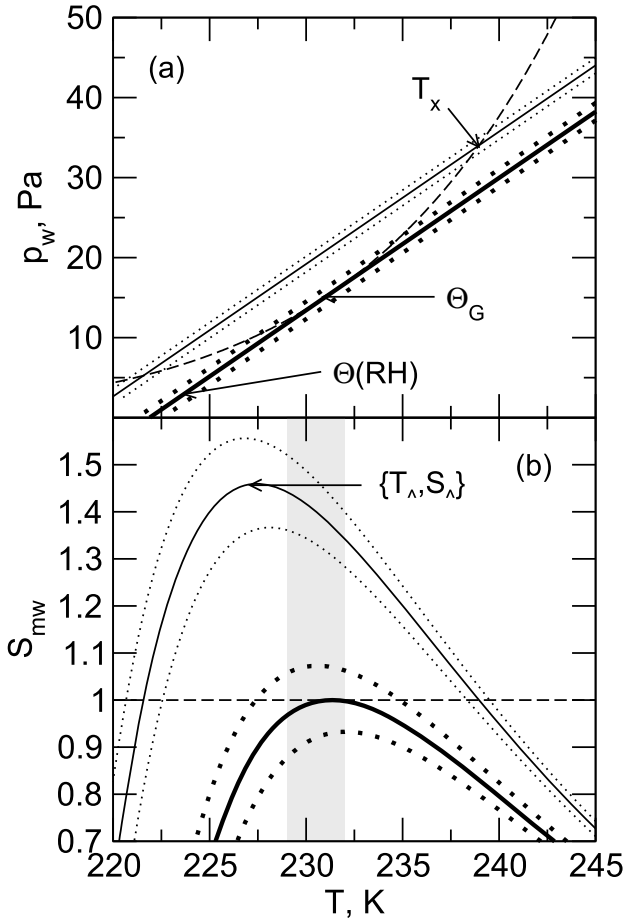

Figure 2. (a) Supercooled water vapor saturation pressure (dashed curve) and average jet plume mixing line (slope $G = 1.64$ PaK^{-1} at $P = 250$ hPa) at the formation threshold temperature for a water-saturated atmosphere ($\Theta_G = 231.2$ K, thick solid line) and below the formation threshold for $T_a = 220$ K in an ice-saturated atmosphere ($\Theta = 224.6$ K, thin solid line) versus plume temperature. The two dotted lines mark shifts of the mixing lines when accounting for uncertainties of humidity and temperature in airborne measurements. (b) Plume water saturation ratio (solid curves) evaluated along the mixing lines. In the "below-threshold" case, imposed experimental uncertainties in temperature and humidity measurements result in variations in the peak S_{mw} values (dotted curves) of $\pm$10 %. The plume becomes water saturated ($S_{mw} = 1$) for the first time at $T_\times = 239$ K, and the peak saturation ratio is reached at $T_\wedge = 227.4$ K. The corresponding results for the threshold case are $\pm$7 % and $T_\times = T_\wedge \simeq \Theta_G$. Homogeneous freezing temperatures of contrail water droplets range between 229 and 232K (gray region). All curves neglect water condensation on plume particles.

heat, Q. The overall efficiency depends on the state of operation of the aircraft via the specific fuel consumption and aircraft speed. A typical value of G is 1.64PaK^{-1} with $\mathcal{M}_w = 1.23$ kg(kg-fuel)$^{-1}$ and $Q = 43.2$ MJ(kg-fuel)$^{-1}$ for conventional jet fuel (kerosene) and for modern aircraft and jet engines in cruise conditions ($\eta = 0.3$ and $P = 250$ hPa). Equation (1) with c_p taken to be constant holds for plume temperatures < 320 K (large plume dilution).

While Θ_G is a function of G only, Θ(RH<100%) additionally depends on T_a for given RH. For a given mixing line slope, the peak plume supersaturation increases with increasing RH and decreasing T_a (Figure 2). The water saturation ratio is defined as the ratio of the partial pressure of water vapor, p_w, to the saturation vapor pressure, $e_w(T)$, over a flat surface taken at the same temperature: $S_w = p_w/e_w$; supersaturation over water is defined by $s_w = S_w - 1$. (Saturation ratios are equivalently defined as corresponding ratios of molecule number concentrations.) Throughout this work, we use the relationships derived by *Murphy and Koop* [2005] to calculate supercooled water and hexagonal ice saturation vapor pressures and associated latent heats of vaporization. When expressed in percent, S_w is identical to relative humidity; in water-supersaturated conditions, $S_w > 1$. In the aircraft plume without condensation, the water saturation ratio, S_{mw}, evolves along the

mixing line, p_{mw}, according to

$$S_{mw} = \frac{p_{mw}(T)}{e_w(T)}, \quad p_{mw} = p_{wa} + G(T - T_a), \tag{2}$$

where p_{wa} is the atmospheric water vapor partial pressure. In contrail-forming conditions, $S_w \leq S_{mw}$ due to possible uptake of water molecules on contrail particles.

Water vapor partial pressures and temperatures measured in the upper troposphere on board research aircraft are associated with experimental uncertainties of at least $\Delta p_w/p_w \pm 10\%$ and $\Delta T \pm 0.5$ K (C. Voigt, personal communication, 2014), respectively, shifting the mixing lines in Figure 2a (dotted lines). This introduces a considerable uncertainty in the estimation of S_{mw}, as illustrated in Figure 2b. The maximum value, 1.07, in the threshold case with imposed uncertainties (thick curves) is much larger than typical atmospheric values of the water saturation ratio at which cloud condensation nuclei activate into water droplets in tropospheric clouds [*Twomey*, 1977]. Peak S_{mw} values exhibit larger shifts with decreasing atmospheric temperature. In the case where T_a is about 5K colder than the threshold so that large plume water saturation ratios are reached (below-threshold case, thin curves), the peak values are sufficiently high (1.35–1.55) enabling the activation of small and hydrophobic aerosol particles that could not serve as cloud condensation nuclei in the atmosphere without those large water saturation ratios seen in aircraft plumes.

The water saturation ratio in the plume would follow S_{mw} if water particles did not form or the uptake of water vapor onto such particles were slow. It is therefore instructive to examine more closely the physical conditions relevant to water condensation during plume mixing. In Figure 3, we depict peak water saturation ratios, $S_\wedge$, and the corresponding temperatures, $T_\wedge$, where those peak values are reached, evaluated along an average mixing line as a function of the atmospheric temperature, T_a. The latter is varied up to the contrail formation threshold temperature, Θ(RH). Taken at $P = 250$ hPa and ice saturation, $\Theta \simeq 224.3$–224.7 K varies slightly with T_a, since RH varies with changing T_a with absolute humidity fixed to ice saturation. For typical conditions at cruise underlying the results shown in Figure 3, $\Theta_G = 231.2$ K. Also shown are the temperatures, $T_\times$, at which the plume first becomes water saturated (before $T_\wedge$ is reached), calculated from

$$S_{mw}(T) = 1\,|_{T=T_\times}; \tag{3}$$

the peak values follow from solving $\mathrm{d}S_{mw}/\mathrm{d}T = 0$:

$$G = S_{mw}(T)\frac{\mathrm{d}e_w}{\mathrm{d}T}\Big|_{T=T_\wedge}, \quad S_\wedge = S_{mw}(T_\wedge). \tag{4}$$

Using $G = 1.64$ PaK^{-1}, $T_\times$ decreases from about 244K toward Θ_G as $T_a \to \Theta$. Since droplet condensational growth can only take place from $T_\times$ onward and T decreases with plume age, this means that the time available for growth decreases with increasing T_a and is zero exactly at the formation threshold for RH = 100% ($T_a = \Theta_G$). At the same time, $S_\wedge$ decreases from about 4 to 1; while the amount of water vapor potentially available for droplet growth increases with decreasing T_a, this amount is zero at Θ_G.

Homogeneous freezing temperatures of supercooled water droplets in tropospheric clouds range between 235 and 239K. In contrails, due to short time intervals supporting freezing and small amounts of liquid water available for freezing, those freezing temperatures happen to be lower as we will show in section 4.2.2. Coincidentally, they are close to Θ_G in upper tropospheric conditions. Therefore, the kinetics of water droplet formation and freezing becomes complicated in "near-threshold" contrails (gray region in Figure 3), where the following set of conditions holds

$$\Theta \to T_a, \quad T_\wedge \to T_\times \to \Theta_G, \quad S_\wedge \to 1. \tag{5}$$

The temporal development of plume supersaturation affects contrail particle formation. Turbulent mixing is responsible for vapor dilution and cooling. Relative changes in p_w and T are similar, because both are affected by the same mixing process, hence the constant slope G of the average mixing line.

We evaluate the total rate of change of S_w in the absence of condensation. The net production rate of supersaturation (supersaturation forcing), $\mathcal{P}_w = \mathrm{d}S_w/\mathrm{d}t$, contains a dilution term reducing p_w that tends to decrease

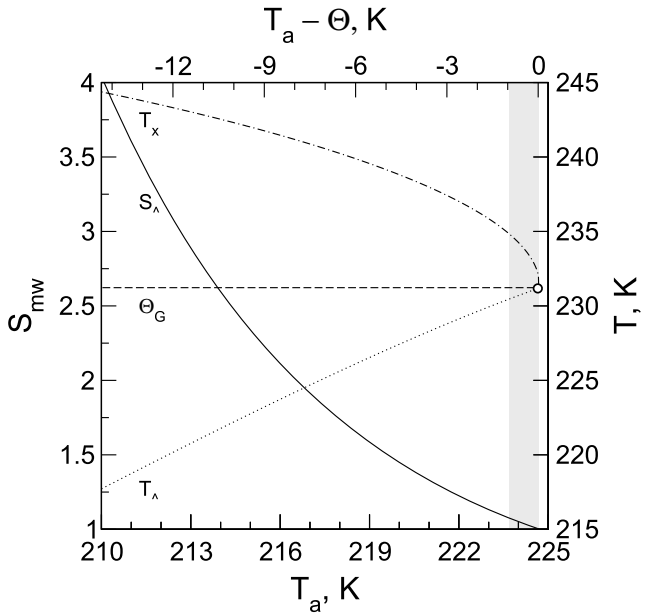

Figure 3. Peak water saturation ratios, $S_\wedge$, and corresponding temperatures, $T_\wedge$, along a plume mixing line with slope $G = 1.64$ PaK^{-1} versus atmospheric temperature, T_a, or the distance, $(T_a - \Theta)$, to the thresholds, $\Theta \simeq 224.3-224.7$ K, taken at ambient ice saturation and $P = 250$ hPa. The Θ_G value at ambient water saturation is also shown together with the temperatures, $T_\times$, at which the plume first becomes saturated with respect to water. The circle marks the conditions exactly at the water saturation threshold, $T_a = \Theta_G$. The region in which $T_\times$ drops sharply toward Θ_G defines a narrow threshold formation zone (gray), where droplet activation and homogeneous freezing are strongly reduced. Curves computed without condensation.

S_w, and a cooling term reducing T and hence the saturation vapor pressure over water, $e_w(T)$, that tends to increase S_w:

$$\mathcal{P}_w = \frac{\mathrm{d}S_{mw}}{\mathrm{d}t} = \left(\frac{G}{e_w} - S_{mw}\frac{L_w}{k_B T^2}\right)\dot{T}\,, \tag{6}$$

where k_B is Boltzmann's constant, $L_w(T)$ is the latent heat of evaporation as embodied in the Clausius-Clapeyron relationship for $e_w(T)$, and $\dot{T} = \mathrm{d}T/\mathrm{d}t < 0$ is the rate of cooling. The first contribution represents the dilution term, and the second contribution represents the cooling term. The net forcing becomes negative when dilution dominates over cooling, later in the jet regime when T falls below $T_\wedge$ (equation (4)).

2.2. Contrail Formation Temperatures

Threshold temperatures, calculated assuming an atmospheric relative humidity corresponding to ice saturation (ensuring contrail persistence) and with the typical value $G = 1.64$ PaK^{-1}, lie below 225K and correspond to altitudes above ~9.5km according to the all-season, midlatitude standard atmosphere. Therefore, threshold temperatures usually lie well below homogeneous freezing temperatures in contrails, hinting at the crucial role of this freezing mode. Weather-induced disturbances, seasonal changes, and latitudinal variations produce local temperature and moisture profiles that can deviate significantly from the standard atmosphere. Therefore, the occurrence of contrails and the cirrus clouds that evolve from them is subject to large meteorological variability [*Burkhardt and Kärcher*, 2009].

If the air is supersaturated with respect to ice and cold enough to support the homogeneous freezing of water droplets, then the contrail water droplets freeze and the resulting ice particles persist, allowing contrails to develop into contrail cirrus [*Schröder et al.*, 2000; *Iwabuchi et al.*, 2012]. Contrails forming only at warmer temperatures persist in the liquid phase at an atmospheric relative humidity of 100%, unless the plume particles act as efficient heterogeneous ice nuclei (section 2.1). In water-saturated air, liquid phase contrails are stable, but natural water clouds would very likely be present. Heterogeneous ice nucleation is indispensable for the further development and possible glaciation of those clouds that might form at lower tropospheric altitudes [*Heymsfield et al.*, 2011].

Contrail water droplets forming at low altitudes evaporate below 100% atmospheric relative humidity. Only if the droplets turn into ice very quickly during the contrail formation process (before the droplets evaporate) can the resulting ice contrails persist over a wide range of RH values down to ice saturation, similar to cold (high-altitude) contrails. This could only happen if emitted soot particles, immersed in supercooled contrail water droplets, are efficient heterogeneous ice nuclei, which as we have argued in section 2.1 can hardly be reconciled with observational evidence.

3. Role of Plume Particles in Contrail Formation

Major plume particle types comprise emitted soot particles and liquid aerosol particles formed within the plume from emitted precursor gases or entrained into the plume from the environmental air. The entrained aerosol may contain insoluble (refractory or nonvolatile) particles that in turn may contain a small subset of efficient heterogeneous ice nuclei, but their number is much smaller than that of the fully liquid (soluble or volatile) particles. In atmospheric measurements, nonvolatile particles are those that leave a residue after being heated to about 500K, while volatile particles completely evaporate at such high temperatures. As a third type of plume particles, ultrafine (nanometer-sized) volatile particles nucleate from the gas phase in the plume before water saturation is reached [*Kärcher*, 1998a, Figure 2]. Their properties depend on concentrations of condensable sulfur species [*Kärcher et al.*, 1998], particulate organic matter, and chemi-ions (charged molecular clusters) [*Yu and Turco*, 1997; *Yu et al.*, 1999] produced from jet fuel combustion.

In an early study, exhaust soot particles have been implicated to play a crucial role in contrail ice formation in threshold conditions [*Kärcher et al.*, 1995]. More recently, distinct regimes have been identified in which aircraft soot emissions play various roles in the formation of jet contrails [*Kärcher and Yu*, 2009; *Wong et al.*, 2013]. In the soot-rich regime, characterized by soot particle number emission indices, EI_s, in excess of $\approx 10^{14}$ (kg-fuel)$^{-1}$, the number of contrail ice particles (then mainly forming on soot particles) increases with increasing EI_s; in this regime, the dependence of contrail properties on the fuel sulfur content is weak. In a transition regime, within the range of $10^{13}-10^{14}$ (kg-fuel)$^{-1}$, the influence of entrained atmospheric aerosol particles on ice formation becomes significant. In the soot-poor regime below $EI_s \approx 10^{13}$ (kg-fuel)$^{-1}$, ultrafine plume particles can be water activated at sufficiently low atmospheric temperatures (leading to high plume supersaturations) and then control the number of contrail ice particles. In the latter regime, the relative contributions to ice formation of the different plume particle types depend, besides on plume and ambient temperatures, on the concentrations of emitted condensable sulfur and organic vapors, and chemi-ions.

3.1. Black Carbon (Soot) Particle Emissions

Chemically impure, refractory particles produced by incomplete combustion of carbonaceous phases are generally referred to as soot [*Bockhorn*, 1994]. Soot particles are composed of pure (elemental) carbon and variable fractions of organic carbon. The rapid formation of solid carbonaceous particles from gaseous hydrocarbons in a combustion chamber is a complex physicochemical process.

After pyrolysis, polycyclic aromatic compounds form in oxygen-poor (fuel-rich) conditions at high temperatures. The aromatic compounds merge to form elementary spherules (diameters 5–10nm) growing further into fractal clusters (geometric mean diameters 15–50nm) by coagulation and condensation processes. At the same time, surface oxidation reduces the mass and number of fresh soot particles. Aircraft-produced primary soot particles are typically smaller than those from other sources and contain sulfate (if the fuel contains sulfur), besides elemental and organic carbon [*Twohy and Gandrud*, 1998; *Petzold and Schröder*, 1998; *Yu et al.*, 1999]. Aircraft soot concentrations seem to show no significant dependence on the sulfur content in conventional jet fuel [*Petzold et al.*, 1997], indicating that sulfur species may be associated with fresh soot particles but do not affect their initial number and size.

Nucleation of ice particles in contrails depends on the number and size of the precursor particles that can be activated into water droplets. Therefore, knowledge of mass emission indices is insufficient to predict contrail microphysical properties. While aircraft soot emissions are relatively well characterized in terms of total mass, data on the number and size of exhaust soot particles in cruising conditions are sparse. Extensive ground-based measurements show marked dependencies of soot emissions on fuel type and engine power setting [*Beyersdorf et al.*, 2014]. In situ measurements combined with an emission inventory model suggest a fleet average soot mass emission index $\mathcal{M}_s \simeq 40$ mg(kg-fuel)$^{-1}$ [*Petzold et al.*, 1999a]. Within the current range of soot number emissions indices at cruise, they are much more abundant by number (at least tenfold) in the

jet plume during contrail particle formation than entrained atmospheric aerosol particles, but significantly less abundant (100-fold or more) than ultrafine volatile plume particles.

Number EIs for aircraft soot particles can be inferred from mass EIs using fixed mass-size relationships such as

$$\mathrm{EI}_s = \frac{3\mathcal{M}_s}{4\pi\varrho_s r_s^3} e^{-(9/2)\ln^2\sigma_s}, \tag{7}$$

with mass density ϱ_s, median radius r_s, and geometric standard deviation, σ_s. Equation (7) arises from the assumption of a unimodal lognormal number size distribution of spherical particles. Although aircraft measurements hint at bimodal soot particle size distributions, comprising a small (primary) mode and a larger (coagulated) mode, this assumption is reasonable (though approximate), since the total number emissions and mean sizes are dominated by the small size mode. The mobility particle size actually measured is close to the size of a volume-equivalent sphere if the particles are sufficiently small (mobility diameters <80–100nm). The mass density, ϱ_s, of aviation soot particles is 1.55gcm^{-3} decreasing with size due to increased porosity; r_s ranges between 20 and 30nm depending on combustor inlet temperature and pressure, and $\sigma_s = 1.6–1.7$ depending only weakly on the soot mass flow rate [*Döpelheuer*, 2002]. Soot emissions are sensitive to the engine thrust [*Anderson et al.*, 2011] and depend on the meteorological situation, which is important for the interpretation of soot emission indices taken in-flight. Predicting EI_s from equation (7) requires accurate r_s values. Variations in r_s and $\mathcal{M}_s$ alone cause in-flight soot number emission indices to lie between 10^{14} and 10^{15} (kg-fuel)$^{-1}$. However, experimental data sets suitable for constraining mass-size relationships for cruising conditions are very limited.

Soot particles from numerous sources, including jet aircraft engine combustors, do not appear to be efficient heterogeneous ice nuclei at upper tropospheric temperatures [*Kärcher et al.*, 2007; *Bond et al.*, 2013]. This means that in order to turn exhaust soot particles into ice, they need to be activated into water droplets that subsequently freeze homogeneously, consistent with the observed wettability of aircraft soot (section 3.2). Direct observational evidence for exhaust soot particles being involved in contrail ice formation was reported by *Petzold et al.* [1998] and *Schröder et al.* [1998], who studied the chemical composition of contrail ice particle residues and observed the in situ evolution of sublimating ice particles in a short-lived contrail, respectively. From the latter study, it was inferred that a significant fraction of the emitted soot particles must have been involved in formation of contrail ice particles.

3.2. Role of Fuel Sulfur in Contrail Formation

Aviation kerosene contains sulfur (S). The fuel sulfur content (FSC) varies widely depending on the origin of crude oils, and the way jet fuel is produced. Average values of FSC amount to several hundreds of milligram S per kilogram of fuel.

Aircraft soot particles are (partially) coated with sulfate and organic compounds already at emission, because these species are produced by rapid chemical reactions during fuel combustion or in the nascent exhaust plume. The coating increases with time after emission by condensation of water and sulfuric acid (H_2SO_4) molecules and by scavenging of ultrafine volatile plume particles [*Kärcher*, 1998b]. Aircraft observations show that changing sulfur emissions only slightly affect contrail properties and only when present in large quantities much in excess of average FSCs.

Enhancing FSC above average values has an effect both on liquid plume particles and on soot particle coatings: the masses of liquid particles and coatings increase due to higher concentrations of hygroscopic sulfuric acid, facilitating water condensation on both particle types and potentially increasing the number of contrail ice particles. Using sulfur-rich kerosene (FSC = 5500 ppmM), contrail color was observed to be slightly altered [*Gierens and Schumann*, 1996] relative to a measurement using fuel with an average sulfur content (170ppmM).

Decreasing FSC was found to have no significant impact on contrail properties. Even a dramatic (100-fold) reduction in FSC (from 250ppmM to only 2ppmM) did not visually affect contrails near the formation threshold [*Busen and Schumann*, 1995]. This means that once a visible contrail forms, a significant fraction of exhaust soot particles must be water activated, even when using almost desulfurized jet fuel. This can be understood by the fact that even hydrophobic graphite can already be partially wetted by adsorption of water molecules slightly below water saturation [*Kärcher et al.*, 1996]. Laboratory-scale measurements show that the

hygroscopicity of aircraft soot particles increases with the sulfur content in the fuel [*Popovicheva et al.*, 2004; *Petzold et al.*, 2005; *Koehler et al.*, 2009]. Aircraft soot may therefore be regarded as insoluble but easily wettable particles with — depending on fuel composition — trace amounts of soluble organic or inorganic matter. In section 3.4 we show how the presence of soluble matter on the surfaces of aviation soot particles increases their hygroscopicity.

3.3. Soluble Plume Particles

Most upper tropospheric particles are composed of supercooled liquid solutions containing water-soluble matter (sulfate and organics, and also nitrate and possibly ammonium) [*Murphy et al.*, 1998]. Physical properties and chemical composition of tropospheric aerosols are highly variable. When entrained into the jet plume, those particles contribute to the contrail ice mass but are too few by number to explain contrail visibility [*Kärcher et al.*, 1996]. Numerical simulations indicate that only when aircraft soot particle emissions were considerably (10–100-fold) reduced, most contrail ice particles form on atmospheric particles entrained into the exhaust plume [*Jensen et al.*, 1998; *Kärcher and Yu*, 2009; *Rojo et al.*, 2015]. Depending on season and location in the upper troposphere, observations point at dry particle sizes (excluding the water fraction) of some 10nm and total number concentrations ranging between 100 and 2500cm^{-3} [*Schröder et al.*, 2002], depending on the presence of a small particle mode.

Volatile plume particles form in the exhaust by gas-to-particle conversion well before the plume reaches water saturation. Microphysical simulations suggest that water activation of those very small soluble particles occurs only at atmospheric temperatures significantly below the threshold temperature and corresponding high plume water supersaturation and only when soot emissions are strongly (at least tenfold) reduced [*Kärcher and Yu*, 2009].

Ultrafine plume particles, which contain dissolved H_2SO_4 and organic matter, require much higher supersaturation over water than larger soot particles in order to activate into water droplets due to their extremely small sizes (mean radii 1–5nm [*Brock et al.*, 2000] depending on FSC). In addition, soot particles (and in their absence, entrained atmospheric particles), which activate already at lower supersaturation (i.e., at a younger plume age), act as a condensation sink for water vapor. Therefore, close to the formation threshold, water vapor does not reach concentrations at which uptake on ultrafine volatile plume particles becomes significant [*Kärcher et al.*, 1995].

Chemical reactions during fuel combustion generate electrically charged, molecular-sized clusters (chemi-ions) [*Yu and Turco*, 1997]. A prominent reaction is $CH + O \rightarrow CHO^+ + e^-$, initiating the production of positively charged organic and negatively charged inorganic molecules. The total number of chemi-ions is controlled by ion-ion recombination reactions and subsequent rapid clustering of H_2O, H_2SO_4, and condensable organic molecules (unburned hydrocarbons) in the cooling plume, leading to a number emission index $(1–4)\times10^{17}$ (kg-fuel)$^{-1}$ of ultrafine volatile particles in cruise conditions, insensitive to wide variations in FSC. Their total number at ground is much (about tenfold) smaller due mainly to faster recombination rates. The clustering leads to nucleation mode particles that stabilize, owing to the very low saturation vapor pressures of their constituent molecules. While neutralizing their charges, the molecular clusters quickly grow to nanometer-sized volatile plume particles mainly by scavenging smaller, molecular clusters forming from binary nucleation of electrically neutral H_2SO_4 and H_2O molecules that were not involved in the ion-mediated nucleation process. The mass growth of ultrafine plume particles can be limited by reducing FSC. By the time the jet plume reaches water saturation, scavenging by emitted soot particles has not yet significantly reduced the total number and mean radii of the ultrafine volatile plume particles, depending on the plume mixing timescale and on FSC.

Prime candidates of particulate organic matter (POM) in those aqueous aerosols are aldehydes (C_nH_{2n+1}–CHO) [*Yu et al.*, 1999]; furthermore, alkenes (C_nH_{2n}) and alkanes (C_nH_{2n+2}) formed by fuel combustion are soluble in aqueous H_2SO_4 solutions and might therefore be present in the ultrafine volatile plume particles, as well as in the soot particle coatings. The detailed chemical speciation of POM is not well known, but the total mass emission index of POM has been estimated to be $\mathcal{M}(\mathrm{POM}) = 20$ mg(kg-fuel)$^{-1}$ [*Kärcher et al.*, 2000]. Emission indices of sulfuric acid amount to 30mg H_2SO_4 (kg-fuel)$^{-1}$, when using fuel with an average FSC of 0.3g S(kg-fuel)$^{-1}$ and a mass conversion fraction 10% of fuel S to H_2SO_4 at emission. The values for $\mathcal{M}$(POM) and S conversion fraction represent average values consistent across many observation cases and may exhibit significant case-to-case variability.

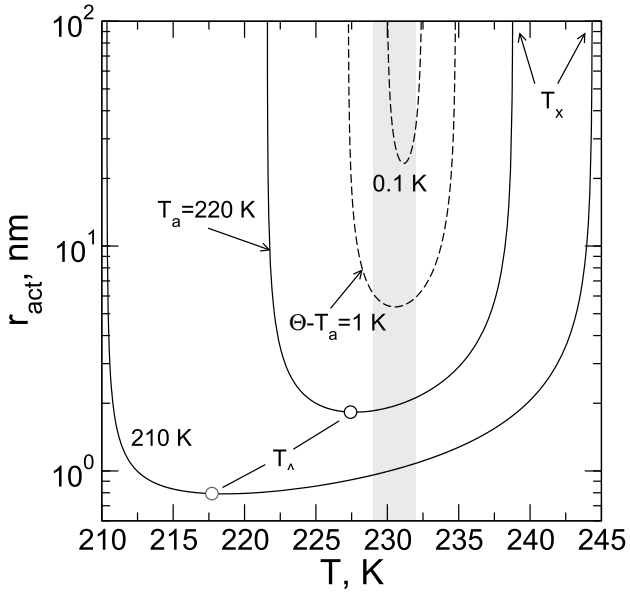

Figure 4. Dry radii of fully soluble aerosol particles that can be activated into water droplets versus plume temperature. The plume water saturation ratio evolves along the mixing line without condensation. Radii are calculated for four atmospheric temperatures, T_a, and $G = 1.64$ PaK^{-1}, $P = 250$ hPa, and ice saturation. The four curves are classified into below-threshold cases (solid curves) and near-threshold cases (dashed curves). All curves have been evaluated assuming rather hygroscopic aerosol. The gray region marks homogeneous freezing temperatures in contrails. Temperatures, $T_\wedge$, at which the plume water saturation ratios take their maxima are indicated for the below-threshold cases. For those cases, the temperatures where the plume first becomes water saturated are $T_\times = 238.8$ K ($T_a = 220$ K) and $T_\times = 244.3$ K ($T_a = 210$ K).

Although current field data suggest that POM constitutes the main particulate mass in ultrafine volatile plume particles only in kerosene with low sulfur content, more research is needed to determine the mass and chemical speciation of POM in ultrafine plume aerosols, including dependencies on flight conditions and fuel composition.

3.4. Solubility Model

The higher the plume supersaturation over water, the easier it is to overcome the Kelvin barrier to condensation and, hence, to activate aerosol particles into nearly pure water droplets. To quantify water activation of soluble plume particles, we employ an analytical parameterization based on Köhler theory, which connects the dry aerosol particle radii, r_{act}, directly with the water saturation ratio, S_w, at which the particles are activated in a supersaturated environment [*Petters and Kreidenweis*, 2007]:

$$\ln(S_w) = \sqrt{\frac{(r_K/r_{act})^3}{54\,k}}\,, \tag{8}$$

where $r_K \simeq 1$ nm is the Kelvin radius held constant in this parameterization. Dry particle cores with radii near r_K require very high supersaturation to activate. The solubility parameter, k, in equation (8) depends on the chemical nature of the solutes, assuming values ≥ 0.6 for very hygroscopic matter comprising sulfuric acid, ammonium sulfate, and ammonium nitrate; k values for aerosol with a composition dominated by organic compounds are lower [*Kreidenweis et al.*, 2009].

We regard this approximate solubility model as a convenient tool to predict the onset of water activation of the various particle types present in jet aircraft exhaust plumes. The use of dry particle radii eliminates the need to solve the Köhler equation which is formulated in terms of total (wet) particle radii. Equation (8) may also be applied to soluble particles containing refractory cores; $k = 0$ for insoluble but wettable particles, although the dependence $\ln(S_w) \propto r^{-3/2}$ changes toward $\ln(S_w) \propto r^{-1}$ as k falls below 0.001. In the case of a mixed particle, an effective k value is defined as the volume-weighted average of k values for the individual components. For coated soot particles with soluble volume fractions on the order of 1% (k value of 0.5), an effective k value for the mixed particle would roughly be $0.5 \cdot 0.01 + 0 \cdot 0.99 = 0.005$. Soluble volume fractions 0.8–1.2% are in line with laboratory-based water activation studies of combustion particles

[*Petzold et al.*, 2005] and vary depending on the sulfur content in the jet fuel. Throughout this work, we use k values 0.5 and 0.005 for fully soluble atmospheric aerosol and coated aircraft soot particles, respectively.

Figure 4 shows the threshold dry radii, r_{act}, of fully soluble aerosol particles, evaluated at $S_{mw}(T)$—the plume water saturation ratio without condensation—using equations (2) and (8). They must be exceeded for particles to be activated into water droplets and therefore made available as homogeneous freezing nuclei in contrails. Since S_{mw} represents the maximum possible saturation ratio, those dry radii are lower limit values. We select two below-threshold cases, with $\Theta \approx 224.5\,\mathrm{K} > T_a = 210$ K and 220K (solid curves), for which the evolution of S_{mw} is shown in Figure 3. Starting at $T = T_\times$, r_{act} values decrease steeply with increasing S_{mw} and reach their minimum values at $T_\wedge$ where the forcing $\mathcal{P}_w$ (equation (6)) changes its sign. At $T < T_\wedge$, r_{act} values increase, as S_{mw} decreases and crosses the saturation point once more (Figure 3b). However, before this can happen, the water droplets freeze homogeneously, i.e., within the gray region (section 4.2.2). This means that the entire region to the left of the freezing zone cannot be populated by supercooled water droplets. Within the freezing zone, all particles cores with dry radii $r_c \gg r_K$ can be activated in contrail-forming conditions.

The situation is different near the formation threshold ($\Theta - T_a < 1$ K). As illustrated with two cases representing near-threshold conditions (Figure 4, dashed curves), activation radii increase rapidly to values > 5–20nm, depending very sensitively on $(\Theta - T_a)$. The peak water saturation ratios are 1.07 [$(\Theta - T_a) = 1$ K] and 1.008 [$(\Theta - T_a) = 0.1$ K]. The corresponding $S_\wedge$ values for the below-threshold cases are 1.45 [$T_a = 220$ K or $(\Theta - T_a) = 4.6$ K] and 4.04 [$T_a = 210$ K or $(\Theta - T_a) = 14.3$ K]. This means that only a fraction of the atmospheric particles (and almost none of the ultrafine volatile plume particles, see next section) can be activated into water droplets very close to the contrail formation threshold. Near the formation threshold, only a very small amount of water is available for condensation, and we therefore expect increasingly fewer droplets to activate as $T_a \to \Theta$. As aircraft soot particles are much less hygroscopic than fully soluble atmospheric particles, their activation radii are substantially smaller; i.e., they activate only at higher supersaturation.

3.5. Summary

For current aviation jet fuel and propulsion technology, aircraft-emitted soot particles trigger ice formation in contrails. We expect a wide range of soot number emission indices during contrail formation, and by inference, variations in initial contrail properties. In usual contrail formation conditions, supersaturation in the plume is high enough to activate most soot particles into small supercooled water droplets despite their poor hygroscopicity. Close to the formation temperature, plume supersaturation diminishes and much fewer particles activate. After being activated, soot cores act as passive inclusions so that freezing occurs by homogeneous nucleation of ice. Solute mass fractions in contrail water droplets are small and do not significantly affect their freezing behavior. Heterogeneous ice nucleation activity of exhaust soot particles is not required to explain contrail occurrence as observed in the upper troposphere. In addition to illustrating the strong control of contrail ice formation by soot emissions, the present study unravels the dependence of initial contrail properties on environmental conditions, first and foremost on ambient temperature. The theory we develop in section 4 is based on the observational evidence and findings as reviewed in this and the preceding section.

If soot emissions from aircraft jet engines were significantly reduced by the use of alternative aviation fuels or advances in engine and propulsion technology, then atmospheric or ultrafine volatile plume particles would trigger ice formation depending on the amount of condensable vapors (mainly H_2SO_4) and atmospheric temperature. The resulting contrails have different microphysical and optical properties. We confine our theory to study contrail ice particle formation on water-activated soot and entrained atmospheric aerosol particles in order to cover contrail formation from conventional and desulfurized alternative aviation fuels, as well as from fuels with strongly reduced soot emissions and volatile particle formation (see discussion in section 6.2).

4. Model Development

Contrail formation processes involve turbulence generated as the exhaust flow interacts with the atmospheric environment by mixing. We first outline the jet plume dynamics (section 4.1) and then develop the microphysical framework (section 4.2). We combine dynamical forcing with the physics of particle formation, growth, and freezing to obtain simple expressions for the total number density and mean radius of contrail water droplets and ice particles nucleating from them by homogeneous freezing. The open circle and the star mark conditions at activation-relaxation and freezing-relaxation, respectively, and the cross marks water-saturated conditions at an earlier plume age (Figure 1b). For ease of notation, subscripts a, m, g, and 0 are introduced

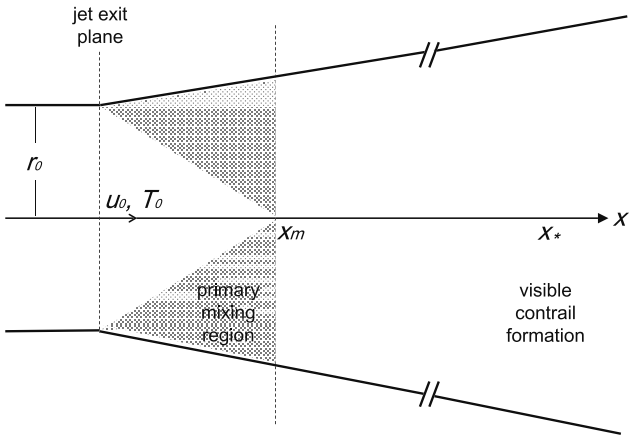

Figure 5. Decay of a free turbulent jet by mixing at constant pressure. The jet exit plane is located at an axial distance $x = 0$, corresponding to the plume age $t = 0$. The jet erodes by entrainment of surrounding air in the primary mixing region (gray). Initial jet radius r_0, initial flow speed u_0, and erosion distance x_m, defining a characteristic mixing timescale, typically several milliseconds, are indicated. Ongoing mixing across streamlines tends to equalize flow variables over the full width of the plume at distances exceeding x_m, causing the plume cross section to increase further. Contrails become visible at a much larger distance $x_\star \gg x_m$ after sufficient cooling, corresponding to a plume age of a few tenths of a second, or less than a wingspan of distance behind the aircraft, although some ice particles may form already in the primary mixing region close to the engine. The jet regime of aircraft wake development lasts a few seconds; then single jets from different aircraft engines merge and are captured in trailing wingtip vortices. The flow of actual aircraft jet engines behind the nozzle exit is surrounded by a sheath of bypass air, and the moving air plane creates a coaxial flow surrounding the jet. Both effects are not shown.

to denote ambient conditions (in the atmosphere outside of the plume), mixing, particle growth, and conditions within the plume at the jet engine exit plane, respectively. Additional subscripts *c*, *s*, *w*, and *i* indicate dry particle core, soot, water, and ice, respectively.

4.1. Jet Plume Dynamics

Turbulent jets have been extensively studied experimentally and theoretically [*Abramovitch*, 1963]. Exhaust effluents exit circular aircraft jet engines in an axisymmetric flow at high speed ($u_0 \simeq 350-450$m/s) relative to the cruise speed of subsonic aircraft (200–250m/s) and at high temperature ($T_0 \simeq 500-600$K) relative to atmospheric temperatures over a range of cruise altitudes 190–270hPa ($T_a \simeq 208-227$K in the extratropics >30°N; $T_a \simeq 217-237$K in the tropics 0°–30°N, based on temperature measurements on board commercial aircraft [*Kärcher et al.*, 2009, Figure 10]). The initial jet carries both thermal and kinetic energy; the latter is quickly dissipated into heat. Turbulence is mainly generated by high shear rates at the boundary between the jet and its environment, causing rapid mixing between exhaust stream and atmospheric air and radial (perpendicular to the flight direction) expansion of the jet plume. The dynamics of jet flow described schematically in Figure 5 and mathematically in section 4.1.2 is simplified in order to obtain an analytically tractable solution that can be coupled with a description of contrail microphysics. For a more detailed accounting of mixing in turbulent shear layers we refer to *Papamoschou and Roshak* [1988]. Mixing causes temperature and number concentrations (per volume of air) of emitted gases and particles to decrease. At the time of contrail formation, the exhaust jets created by different aircraft engines have not yet merged. Therefore, it is appropriate to study the dynamics of single jets in the context of contrail formation microphysics. During the short time of contrail formation, ambient atmospheric conditions are assumed to stay constant.

To a very good approximation, subsonic jets evolve isobarically, since the exhaust air expands very quickly to atmospheric pressure near the nozzle exit of a subsonic jet engine. Because of the short lifetime of aircraft jet plumes, buoyancy and radiative cooling do not significantly affect their development. Constant emission and flow conditions result in a steady state flow field and the evolution of the jet rapidly approaches a state of self-similarity in the main thermodynamic (temperature and moisture content) and dynamic (flow velocity) variables relevant to contrail formation. This means that radial profiles of a flow variable, or any passive tracer, at any axial location become asymptotically independent of the initial profile and can be obtained by scaling the profiles at another location. (For a self-similar flow variable f, $f(x, y) \propto F[y/g(x)]$, with a scaling function $g(x)$. In the case of the axial velocity field of a free circular jet, $g(x) = (4\epsilon/\sqrt{3})\,x$ and $F = 1/[1 + (y/g)^2/4]$,

where ϵ is a dimensionless turbulent diffusivity [*Kärcher and Fabian*, 1994].) The jet regime lasts for a few seconds and ends when the exhaust plumes start to be trapped in the developing wingtip vortices. The vortices tend to descend a few hundreds of meters below the flight level, and the resulting adiabatic heating may cause some contrail ice particles to sublimate, even for slightly ice-supersaturated ambient conditions. The vortex regime wherein mixing is strongly suppressed lasts for a few minutes and is terminated by dissipation induced by mixing with a large volume of atmospheric air [*Miake-Lye et al.*, 1993; *Kärcher*, 1999]. Contrary to the vortex and dissipation regimes, the development of which depends on many aircraft (e.g., size and weight) and atmospheric parameters (e.g., lapse rate and wind shear), the jet regime is universally described by only a few parameters.

4.1.1. Mixing Timescale

In the initial jet, the inner region retains its high speed, temperature, and species concentrations longer than outer plume regions (Figure 5). The jet erodes with increasing axial distance from the exit plane, x. The length, x_m, denotes the maximum distance over which the central jet region is unaffected by entrainment. The associated mixing timescale, τ_m, is defined as the time a volume element of exhaust located at the center of the jet plume needs to reach x_m:

$$x_m \simeq r_0\sqrt{2/\epsilon}\,, \quad \tau_m \simeq x_m/u_0 \tag{9}$$

[*Kärcher and Fabian*, 1994], where r_0 is the initial jet radius and $\epsilon = 0.0285$ is the value of the dimensionless turbulent diffusivity (in units of $r_0 u_0$) inferred from experimental data [*Tollmien*, 1926]. When using $r_0 = 0.5$ m, we obtain $x_m \approx 4$ m and $\tau_m \approx 10$ ms, as estimates for the characteristic distance behind the engine exit plane and associated time needed for the flow field to enter the fully turbulent regime ($x > x_m$) after a narrow transition region.

4.1.2. Cooling Rate and Dilution Factor

We track the dilution history of air parcels emanating from the jet engine within the center region of the nozzle exit plane and regard those bulk plume properties as appropriate for the description of contrail particle formation.

As the mean turbulent flow field is in steady state for constant u_0 and T_0, the time t elapsed corresponds to the age of the plume represented by the streamline at the jet center. The cooling rate, $\dot{T}$, of the central jet region evolves with time $t > \tau_m$ according to

$$\dot{T} \equiv \frac{\mathrm{d}T}{\mathrm{d}t} = -\omega(t)(T - T_a)\,, \quad \omega = \frac{\beta}{t}\,, \tag{10}$$

with the dilution parameter $\beta \simeq 0.9$ [*Kärcher*, 1999, Figure 4], the entrainment (dilution) rate, ω, the plume temperature, T, and the atmospheric temperature, T_a; at $t < \tau_m$, $\omega = 0$.

Integrating equation (10) using $T(t \le \tau_m) = T_0$ leads to the temperature history

$$T(t) = T_a + (T_0 - T_a)\mathcal{D}(t)\,, \quad t > \tau_m\,, \tag{11}$$

with the dilution factor $\mathcal{D}$

$$\mathcal{D}(t > \tau_m) = \exp\left(-\int_{\tau_m}^{t} \omega(t')\mathrm{d}t'\right) = \left(\frac{\tau_m}{t}\right)^{\beta}; \tag{12}$$

at $t \le \tau_m$, $\mathcal{D} = 1$. The dilution factor provides us with explicit information about the temporal evolution of the mixing process affecting the plume center region and is a prerequisite for the evaluation of contrail microphysics (section 4.2). The circular plume cross-sectional area, A, increases with time according to $A(t) = A_0/\mathcal{D}(t)$, implying that the diameter of the whole plume follows from $d = d_0/\sqrt{\mathcal{D}}$, where d_0 is the jet engine diameter. Knowledge of d is useful for estimates of the contrail optical depth.

Combining equations (11) and (12), the plume dilution factor and cooling rate can be written as a function of T,

$$\mathcal{D} = \frac{T - T_a}{T_0 - T_a}\,, \tag{13}$$

$$\dot{T} = -\beta\frac{(T_0 - T_a)}{\tau_m}\mathcal{D}^{1+1/\beta}\,, \tag{14}$$

and the plume age is related to the plume temperature via

$$t = \tau_m \left(\frac{T_0 - T_a}{T - T_a} \right)^{1/\beta} . \tag{15}$$

Equations (10)–(15) are valid up to the end of the jet regime. The maximum time, δt, available for condensational growth of the water droplets before freezing, follows from equation (15) as the difference in the plume ages where water saturation is reached, $t_\times$, and the freezing-relaxation commences, $t_\star > t_\times$ (Figure 1b):

$$\delta t = t_\star - t_\times = \tau_m \left[\left(\frac{T_0 - T_a}{T_\star - T_a} \right)^{1/\beta} - \left(\frac{T_0 - T_a}{T_\times - T_a} \right)^{1/\beta} \right] . \tag{16}$$

It is an important coincidence that homogeneous freezing temperatures, $T_\star$, are only slightly lower than $T_\times$ (section 4.2.2). For this reason, δt is very short and zero exactly at the formation threshold (section 2.1). For instance, with $T_0 = 600$ K, $T_\times = 240$ K, $T_a = 220$ K, $\beta = 0.9$, and $\tau_m = 10$ ms, we find $\delta t \simeq 0.2$ s for an estimated freezing temperature $T_\star = 231$ K.

The thermodynamic approach employs a mass-based mixing factor, $\mathcal{N}$, as a measure of plume mixing (air-to-fuel ratio), however, without considering an explicit time dependence of the mixing process. It is linked to our dilution factor via $\mathcal{D} = \mathcal{N}_0/\mathcal{N}$ for $t \gg \tau_m$. At the jet engine exit plane, $\mathcal{N} = \mathcal{N}_0 > 1$; the fuel is usually burnt under excess air conditions, so that the exhaust leaves the jet engine already diluted. Typical values are $\mathcal{N}_0 = 50–70$.

4.1.3. Emission Indices

We introduce the number emission index (EI) as a convenient concentration measure of emitted species (molecules or particles). The EI, in units of (kg-fuel)$^{-1}$, is invariant under changes of the plume volume due to mixing, contrary to the number concentration per unit air volume, n:

$$\mathrm{EI} = \frac{\mathcal{N}_0}{\mathcal{D}} \frac{n}{\varrho} , \tag{17}$$

where $\varrho(P, T)$ is the mass density of air. Should n become comparable to its concentration in ambient air (if present), then it must be replaced by the difference between n and its ambient level. As mixing is isobaric, the partial pressure of any gaseous or particulate plume constituent evolves along the mixing line in the absence of condensation or chemical reactions. Therefore, mixing ratios (partial pressures) of species dilute at the same rate as the temperature cools. Equation (17) can be applied to define apparent number emission indices, AEI_i, for contrail ice particles created past emission. In this way, their number can be defined irrespective of plume dilution and can thus be directly compared to the number of precursor particles upon which they form.

We also define an apparent number emission index for aerosol particles entrained into the plume from the surrounding air:

$$\mathrm{AEI}_a = \mathcal{N}_0 \frac{T_a}{T} \frac{1 - \mathcal{D}}{\mathcal{D}} \frac{n_a}{\varrho} . \tag{18}$$

Here n_a is the total (ambient) number concentration of atmospheric particles mixed into the plume. The temperature ratio in equation (18) converts between plume number concentrations and mixing ratios. The $\mathcal{D}$ ratio accounts for the fact that the number mixing ratio of entrained species, χ, is given by $\chi = \chi_a(1 - \mathcal{D})$, which follows in analogy to equations (10) and (11) with $\chi_0 = 0$. Both are time dependent and will later be taken at the plume age where contrail particles form.

Based on equations (17) and (18), we define a contrail exhaust regime parameter,

$$\xi = \mathrm{EI}_s / \mathrm{AEI}_a , \tag{19}$$

in order to judge whether aircraft-emitted soot particles dominate the droplet (and therefore the ice particle) number budget in contrails (section 3). Setting $n_a = 1000$ cm^{-3}, the contrail regime is soot rich if $\xi > 1$, translating into $\mathrm{EI}_s > 5 \times 10^{12}$ (kg-fuel)$^{-1}$ using $\mathcal{N}_0 = 60$, $P = 250$ hPa, $T \simeq T_\star = 231$ K, and $T_a = 220$ K. All regime parameters introduced in this work are summarized in Table 1.

Table 1. Regime Parameters Describing Salient Features of Contrail Microphysics in Jet Exhaust Plumes

Parameter	Meaning	Definition	Limits		Role	Value/Range[a]
			$\gg 1$	$\ll 1$		
ξ	exhaust regime	equation (19)	soot rich[b]	soot poor[c]	relates contrail particle number to soot emissions	>10–100
ψ	condensation regime	equation (31)	fast droplet growth[d]	slow droplet growth[e]	determines freezing droplet size	>1
λ	freezing regime	equation (35)	all droplets frozen	no droplets frozen	determines homogeneous freezing temperature	~1
κ_w	activation-relaxation	equation (49)	fast droplet growth[d]	slow droplet growth[d]	determines droplet number	< 0.1 to > 10
κ_i	freezing-relaxation	equation (34)	fast ice growth[e]	slow ice growth[e]	determines ice particle number	<1

[a]Typical value in jet contrails during droplet or ice formation.
[b]Relative to number concentration of atmospheric nuclei, n_a.
[c]Relative to maximum time available for droplet growth, δt.
[d]Relative to duration of droplet activation pulse, τ_{act}.
[e]Relative to duration of droplet freezing pulse, τ_{frz}.

4.1.4. Uncertainties

Complications not captured in our approach arise due to the core/bypass structure of real jet engines: a sheath of slower, colder air surrounds the jet core. Contrary to the high speed jet core, the coaxial sheath contains mainly (mildly heated) ambient air. For engines with high bypass ratios, the bypass flow contains several times the air mass of the engine core. In some engines, bypass and core flow are premixed. Bypass and core flow are associated with different axial velocities. Mixing causes the sheath layer to merge with the atmospheric flow and the exhaust core well before the formation of a visible contrail is completed, creating a relatively uniform, self-similar jet flow. Finally, the jets are embedded in an atmospheric coflow affecting the plume dynamics. Since contrails become clearly visible in the fully developed, turbulent flow regime only after substantial plume mixing (Figure 5), these modifications only affect the flow close to the nozzle exit and are unlikely to cause major uncertainties in our analysis. Capturing such fluid dynamical details may be more important for accurate predictions of shape and width of the ice particle size distribution, but it is unlikely that they substantially affect the plume-averaged, total contrail ice particle number concentration and mean size.

Our concept to simplify the dynamics of jet plumes in order to develop a minimal model for the microphysics of contrail formation recognizes the fact that timescales for mixing and cooling, droplet activation and growth, and ice nucleation and growth are similar [*Kärcher*, 1998a]. It does not explicitly account for plume inhomogeneities caused by radial gradients of physical variables and effects of turbulence on microphysical processes other than those embodied in the bulk entrainment rate that is representative for mixing of the jet core. Those inhomogeneities translate into variability in temperature and moisture content (section 2.1), affecting the cooling rate and the microphysics of water uptake on, and subsequent freezing of, plume particles. For instance, numerical simulations of free turbulent jets indicate that fluctuations in S_w of up to several tens of percent can be caused by radial mixing in the primary mixing region close to the jet boundaries for a jet engine with a bypass [*Kärcher*, 1994; *Kärcher et al.*, 1996]. Large eddy simulations show that air parcels originating at different radial locations of a jet exit plane experience different microphysical histories forced by exposure to a wide range of turbulent plume conditions [*Paoli et al.*, 2004, 2013]. The resulting flow inhomogeneities might lead to the formation of some ice particles behind a real jet engine much earlier than the time needed to produce a contrail that is visible by a distant (e.g., ground-based) observer.

4.2. Droplet and Ice Microphysics

We extend a previous study of ice formation in contrails [*Ford*, 1998] by including plume particles as water condensation nuclei and contrail droplet activation and growth processes. We assume that the thermodynamic criterion for contrail formation is met at a temperature, T_a, lower than the threshold temperature, Θ, for given air pressure, atmospheric relative humidity, and aircraft/engine/fuel parameters. This implies that the relative humidity in the jet plume surpasses water saturation, allowing the activation of plume particles into water droplets. Contrail ice particles nucleate from those water-activated particles by homogeneous freezing,

the dominant ice formation mode at low temperatures. Contrail water droplets and ice particles are treated as monodisperse populations characterized by total number densities, n, and (mean) radii, r. The humidity in the atmosphere surrounding the jet plume does not directly affect the droplet and ice formation microphysics, since at the time contrail particles form (at plume ages below 1s), the plume moisture content is still dominated by the emitted water vapor (Figure 2b), and the entrainment of the comparatively low levels of upper tropospheric water vapor is quite unimportant. Nonetheless, the ambient relative humidity affects the threshold temperature. The difference between the threshold temperature and the ambient temperature strongly impacts the thermodynamic plume conditions prevailing during droplet activation and freezing (Figures 3 and 4).

We begin by providing a rough estimate for mean droplet radii (section 4.2.1) in order to estimate homogeneous droplet freezing temperatures in contrails (section 4.2.2). Finally, the activation-relaxation process is analyzed (section 4.2.3) determining the number concentrations and mean sizes of contrail droplets available for freezing.

4.2.1. Droplet Growth

To arrive at a rough estimate for the droplet radius r_w, we introduce a few simplifying assumptions. The droplet number concentration, n_w, is assumed to be known; it will be derived consistently with droplet size and supersaturation forcing in section 4.2.3. We assume that plume particles activate into water droplets at $T_\times$, growing and depleting the water vapor at constant temperature until homogeneous freezing occurs, i.e., within the maximum available growth time, δt. These assumptions allow us to solve the set of condensation-growth equations analytically:

$$n_w^{\mathrm{sat}} \frac{\mathrm{d}s_w}{\mathrm{d}t} = -\mathcal{J}_w n_w \,, \quad s_w(t=0) = s_{mw} \,, \tag{20}$$

$$4\pi r_w^2 \frac{\mathrm{d}r_w}{\mathrm{d}t} = v\mathcal{J}_w \,, \qquad r_w(t=0) = r_c \,, \tag{21}$$

where $n_w^{\mathrm{sat}}(T)$ is the H_2O number concentration at water saturation, v is the volume of an H_2O molecule in supercooled water, and

$$\mathcal{J}_w = \frac{\pi r_w^2 \alpha_w v s_w n_w^{\mathrm{sat}}}{1 + \alpha_w v r_w/(4D)} \tag{22}$$

is the flux (per unit time) of water molecules to the droplets [*Pruppacher and Klett*, 1997]. We introduce a correction factor in the denominator of $\mathcal{J}_w$ accounting for the fact that droplet growth might become governed by gas diffusion and we omit the lowering of the saturation vapor pressure over the curved surfaces of the water-activated droplets. Therefore, r_w values are upper limits. In equation (22), $v(T)$ is the mean thermal speed of water molecules, $D(P, T)$ is their diffusion coefficient in air, and $\alpha_w = 1$ their accommodation coefficient.

A first integral of equations (22) and (23), expressing water mass conservation, is given by

$$s_w(r_w) = s_{mw} + \frac{4\pi n_w}{3v n_w^{\mathrm{sat}}} \left(r_c^3 - r_w^3\right) \,, \tag{23}$$

from which the maximum possible droplet radius, $R = r_w(s_w = 0)$, can be derived:

$$R^3 = r_c^3 + \frac{3v s_{mw} n_w^{\mathrm{sat}}}{4\pi n_w} \,. \tag{24}$$

The second term on the right-hand side of equation (24) is a measure of the maximum volume of condensable water vapor.

There are only two parameters governing the kinetics of water vapor condensation: the dimensionless ratio

$$Z = \frac{4\pi n_w R^3/3}{v s_{mw} n_w^{\mathrm{sat}}} = 1 + \frac{4\pi n_w r_c^3/3}{v s_{mw} n_w^{\mathrm{sat}}} \geq 1 \,, \tag{25}$$

of the total particle volume and the maximum condensate volume and the supersaturation relaxation timescale

$$\tau_S = \frac{3Z}{\alpha_w v \pi R^2 n_w}\,, \tag{26}$$

as the characteristic time to deplete the water vapor above water saturation, if there were no forcing of supersaturation.

Introducing dimensionless quantities (marked $\tilde{(\cdot)}$) and using s_{mw}, R, and τ_S as scaling variables, it is straightforward to show that the second (radial growth) integral, arising from equation (23), takes the scaled form

$$Z\delta\tilde{t} = \int_{\tilde{r}_c}^{\tilde{r}_w} \frac{1+qz}{1-z^3}\mathrm{d}z\,,\ q = \frac{\alpha_w v R}{4D}\,,\ \tilde{r}_c = \left(1-\frac{1}{Z}\right)^{1/3}\,. \tag{27}$$

After solving equation (27) and inversion to obtain upper limit values $\tilde{r}_w$ constrained by the maximum available growth time, $\delta\tilde{t}$, from equation (16), the mean droplet radius, water supersaturation, and liquid water volume at plume age t follow from

$$r_w = R\tilde{r}_w\,, \tag{28}$$

$$s_w = s_{mw} Z(1-\tilde{r}_w^3)\,, \text{ and} \tag{29}$$

$$\mathrm{LWV} = 4\pi\left(r_w^3 - r_c^3\right)/3\,. \tag{30}$$

Equations (32)–(34) constitute the approximate conditions of plume moisture and liquid condensate as time evolves after activation of droplets with total number concentration n_w.

We introduce the condensation regime parameter

$$\psi = \delta t/\tau_S\,. \tag{31}$$

If water condensation is fast ($\psi \gg 1$), then $r_w \propto 1/n_w^{1/3}$, decreasing with n_w, since the same amount of condensate is distributed among more droplets. For slow condensation ($\psi \ll 1$), the final droplet radius approaches a value independent of n_w but limited by the available growth time, i.e., $r_w \propto \delta t$. In contrails forming well below the threshold, condensation is typically fast: $r_w \gg r_c$. On the contrary, at the contrail formation threshold, $s_{mw} \to 0$, and therefore $r_w \to r_c$.

Those features are illustrated in Figure 6, where we show the droplet radii, r_w, and the condensation regime parameter, ψ, as a function of assumed droplet number concentrations expressed in terms of a number emission index, EI_w, using equation (17). We vary EI_w over the greatest conceivable range of values, encompassing very low ambient or very high emitted soot particle concentrations. The curves were evaluated at an estimated homogeneous freezing temperature of 231K. The initial droplet (core particle) radius was set to $r_c = 0.03\,\mu\mathrm{m}$; otherwise, we use the standard set of parameters (leading to $\delta t \simeq 0.2$ s). For comparison, the maximum possible droplet radius, R, is shown alongside r_w.

Condensation is fast, if $\mathrm{EI}_w > 5 \times 10^{13}$ (kg-fuel)$^{-1}$, including typical values of current EI_s, in which case r_w decreases with EI_w, as noted above. For lower droplet concentrations, r_w assumes a constant value, since condensation is limited by the available growth time; the comparison with R demonstrates that the freezing droplets then contain much less water than available in the plume.

This analysis shows that for current soot emission levels, water condensation in jet plumes in below-threshold contrails at the point of ice formation is typically fast, and $r_w = 0.3$–$0.5\,\mu\mathrm{m}$. The value of EI_w in Figure 6 where $\psi = 1$ corresponds to an atmospheric aerosol particle number concentration $n_a \simeq 1000\,\mathrm{cm}^3$ (equation (19)). This means that in cases where contrails mainly form on entrained aerosol particles, droplet growth may often be kinetically controlled, limiting the initial contrail ice particle radii to values of about $0.6\,\mu\mathrm{m}$. Kinetic limitations also occur in near-threshold contrails, where only few droplets form owing to very small supersaturations.

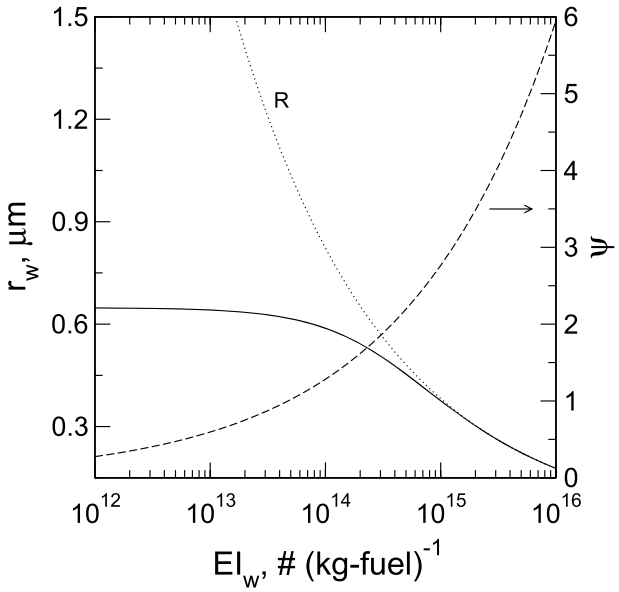

Figure 6. Approximate freezing droplet radii (solid curve) and condensation regime parameter (dashed) as a function of water droplet number emission indices. The maximum possible droplet radii that would result from condensing all available water vapor in the plume are shown in comparison (dotted). We use the standard set of model parameters: ambient ice saturation at $P = 250$ hPa and $T_a = 220$ K; $T_0 = 600$ K, $\beta = 0.9$, and $\tau_m = 0.01$ s; $T_\times = 240$ K and $T_\star = 231$ K.

4.2.2. Freezing-Relaxation

Homogeneous ice formation is described in terms of the freezing rate of supercooled water, $j = \mathrm{LWV}{\cdot}J$, defined as the product of the freezing rate coefficient, J (number of ice germs nucleating per unit droplet volume per unit time), and the liquid water volume available for freezing, LWV. Assuming that the entire droplet freezes instantly once ice nucleates within its volume, j yields the number of droplets freezing per unit time.

The assumption of a freezing pulse, $j(t)$, is reasonable, since prior to the time of freezing ice formation is suppressed, because it is too warm for ice to form ($J \approx 0$). With increasing plume age, as temperatures become sufficiently low, J will increase very rapidly maximizing at the time of freezing-relaxation. Beyond that time, j will also be negligible because all droplets froze or the remaining droplets evaporate (LWV ≈ 0), meaning that j decays rapidly beyond the time of freezing-relaxation. The pulse-like nature of j may be modeled by a characteristic timescale, τ_{frz}:

$$\tau_{\mathrm{frz}}^{-1} \equiv \frac{\partial \ln(j)}{\partial t} \simeq \frac{\partial \ln(J)}{\partial T}\dot{T}\,, \tag{32}$$

neglecting the rate of change of ln(LWV) relative to that of ln(J). We have already derived an expression for the bulk cooling rate, $\dot{T}$ (equation (15)). We compute $J(T)$ from a parameterization based on recent laboratory measurements [*Riechers et al.*, 2013]:

$$\ln\left(J\left(\mathrm{cm}^{-3}\,\mathrm{s}^{-1}\right)\right) = a_1 T + a_2\,, \tag{33}$$

with $a_1 = -3.5714\ \mathrm{K}^{-1}$ and $a_2 = 858.719$. Equation (33) is an accurate approximation of the freezing rate of supercooled, pure water at temperatures around 235K, stating that J increases by a factor $\exp(-a_1) \approx 35.6$ upon a decrease in T by 1K. Uncertainties in J as quantified by *Riechers et al.* [2013] have no significant impact on $\tau_{\mathrm{frz}} = 1/(a_1\dot{T})$.

Ford [1998] has shown for fixed droplet properties that to a good approximation, ice particle growth is slow relative to freezing so that all droplets tend to freeze before they start to grow and deplete the vapor. This follows from the freezing-growth regime parameter

$$\kappa_i = \frac{\tau_{\mathrm{frz}}}{\tau_{gi}}\,, \quad \tau_{gi}^{-1} = \frac{b_1/r_w}{1 + b_2 r_w}\,, \tag{34}$$

with $b_1 = v\alpha_i v s_i n_i^{\mathrm{sat}}/4$, where s_i is the supersaturation over ice taken at water saturation and α_i is the deposition coefficient for H_2O molecules impinging on the ice surfaces, and $b_2 = v/(4D)$. The dynamical regime

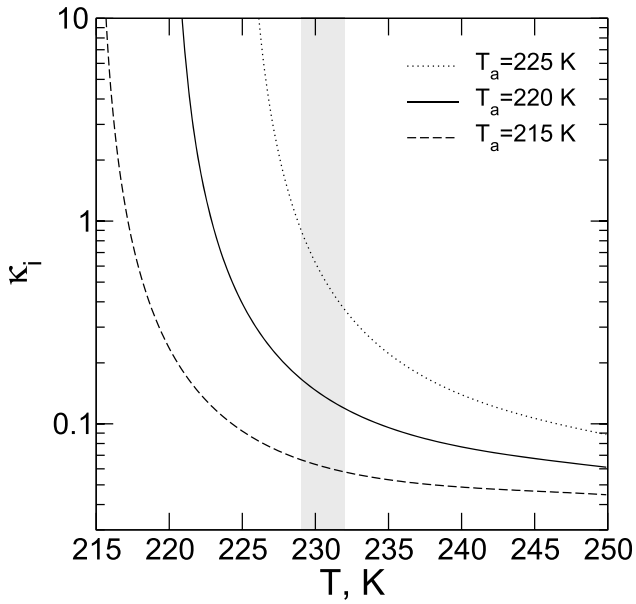

Figure 7. Freezing-growth regime parameter versus temperature in plumes expanding at various ambient temperatures, evaluated at 250hPa and using $r_w = 0.4\,\mu m$, $T_0 = 600$ K, $\beta = 0.9$, and $\tau_m = 0.01$ s. The gray region marks the range of estimated homogeneous freezing temperatures in contrails.

parameter, κ_i, measures the time scale of the freezing event (equation (32)) relative to the initial ice particle growth time scale, τ_{gi}, defined applying equation (22). Setting $\alpha_i = 1$ is justified owing to the high supersaturations over ice at the time of freezing. The regime parameter is shown in Figure 7, evaluated for various ambient temperatures and $r_w = 0.4\,\mu m$. The general increase in κ_i with decreasing T reflects its dependence on the cooling rate, which rapidly approaches zero as $T \to T_a$. At temperatures where homogeneous freezing occurs (gray area), the slow growth regime is realized in all cases (as $\kappa_i < 0.5$); the highest value is attained near the formation threshold at $T_a = 225$ K. At extratropical cruise altitudes, lower atmospheric temperatures are more common and κ_i values are much smaller. In near-threshold cases where the slow growth condition is not realized, assuming all droplets to freeze would overestimate the number of ice particles.

We evaluate the dimensionless parameter

$$\lambda = \mathrm{LWV} J \tau_{\mathrm{frz}} = \frac{4\pi}{3}\left(r_w^3 - r_c^3\right)\frac{J}{a_1 \dot{T}} \tag{35}$$

with the droplet radii, $r_w(T) \geq r_c$, where r_c is the radius of the dry aerosol core upon which the droplets form. In essence, λ is equal to the frozen droplet fraction, n_i/n_w. Consistent with the slow growth regime (nucleation burst) scenario, we can therefore infer the temperature at freezing-relaxation, $T_\star$, by inverting $\lambda(T_\star) = 1$. To a first approximation, we evaluate this relationship at a constant cooling rate leading to

$$T_\star \simeq \frac{1}{a_1}\left[\ln\left(\frac{a_1 \dot{T}}{V_w}\right) - a_2\right] \tag{36}$$

with the single droplet volume $V_w = 4\pi r_w^3/3$ and $r_c = 0$. Assuming $\dot{T} = -25\ \mathrm{Ks}^{-1}$ and $r_w = 0.4\,\mu m$, we find $T_\star \approx 231$ K as a rough estimate of the homogeneous freezing-relaxation temperature in jet contrails, significantly lower than in natural clouds where cooling rates are much slower and droplet volumes much larger. The dependencies on $\dot{T}$ and V_w form the basis of the estimated range of freezing temperatures as indicated in Figure 7.

We estimate $T_\star$ more accurately as a function of r_w using $r_c = 0.02\,\mu m$ and the cooling rate from equation (15). The results shown in Figure 8 show that $T_\star = 229$–232 K in contrails. Decreasing T_a increases $|\dot{T}|$; as for decreasing r_w, the resulting decrease in λ is compensated by lowering $T_\star$ (increasing J). Changing parameters other than T_a and $(r_w - r_c)$ has a very small impact on $T_\star$. Only in near-threshold contrails, where the liquid water volume can become very small (as $r_w \to r_c$), homogeneous freezing temperatures decrease notably falling below $\Theta_G \approx 231$ K (section 2.1).

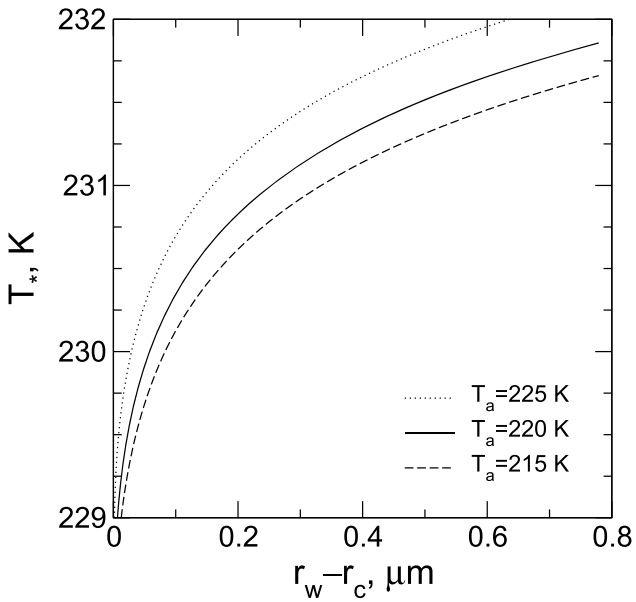

Figure 8. Homogeneous freezing temperatures in contrails versus freezing droplet radii, estimated from the regime parameter λ assuming droplet cores with $r_c = 0.02\,\mu m$ for a range of ambient temperatures. The underlying plume cooling rate was evaluated using $T_0 = 600$ K, $\beta = 0.9$, and $\tau_m = 0.01$ s and varies with T_a.

4.2.3. Activation-Relaxation

We determine the total number concentration, $n_\circ$, and mean radius, $r_\circ$, of contrail water droplets along with plume conditions at the time $t_\circ$ when supersaturation relaxation occurs (*i.e.*, at the point of 'activation-relaxation'). We cannot rely on the growth model equations (32)–(34), as this model requires the droplet number as input and does not consider forcing of supersaturation. However, the number of activated droplets must be determined self-consistently with both supersaturation forcing and depletion due to droplet condensational growth.

Our concept of 'activation-relaxation' rests on the idealization that, with increasing supersaturation, $s_w(t) = s_{mw}(T)$, determined by plume cooling ($T_\wedge < T < T_\times$), condensation nuclei will activate into water droplets without affecting the evolution of s_w up to the instant, $t_\circ$, where the number of already activated droplets has increased to a value, $n_\circ$, sufficiently large to quench the supersaturation. The quenching is assumed to occur instantly so that no further activation occurs after $t_\circ$. The latter assumption is robust, inasmuch as nuclei that have already been activated at $t < t_\circ$ are no longer available for activation in the declining supersaturation at later times. The former issue (s_w unaffected by early activated nuclei) might become relevant for ultrafine volatile plume particles, since even very small reductions in s_w at $t < t_\circ$ can affect their activation behavior at $t = t_\circ$, because their dry radius is close to the Kelvin radius (section 3.3). Owing to their much larger dry sizes, we argue that this is less of an issue for emitted soot and entrained atmospheric particles.

Before we determine $n_\circ$, we estimate the number concentration of contrail droplet nuclei that activate into water droplets at any given plume supersaturation. To this end, we make use of the solubility model (section 3.4), yielding the dry radii $r_{act}(s_w)$ at which core particles with $r_c > r_{act}$ can be considered water activated controlled by the effective solubility parameter, k.

The total droplet number concentration is obtained by adding the contributions from soot emissions and entrained atmospheric particles:

$$n_w^{(1)} = \varphi_s \underbrace{\mathrm{EI}_s \frac{\varrho \mathcal{D}}{\mathcal{N}_0}}_{n_{ws}} + \varphi_a \underbrace{\frac{T_a}{T}(1-\mathcal{D}) n_a}_{n_{wa}} \tag{37}$$

according to equations (17) and (18), where n_{wl} denotes the total number concentration of plume particle type $l = s, a$ at temperature T. The fractions $\varphi_l(s_w)$ determine the cumulative contributions of water-activated type l particles relative to n_{wl}. To estimate φ_l, we characterize each plume aerosol type by a normalized lognormal

size distribution:

$$\frac{\mathrm{d}n_{wl}}{\mathrm{d}r} = \frac{n_{wl}}{\sqrt{2\pi}\ln\sigma_l}\frac{1}{r}\exp\left[-\frac{\ln^2(r/\bar{r}_l)}{2\ln^2\sigma_l}\right], \tag{38}$$

where r is the dry particle radius and $\bar{r}_l$ and σ_l indicate the prescribed geometric mean dry radius and standard deviation, respectively. The dry radii of type l particles activating at $S_w > 1$ follow from equation (8):

$$r_{\mathrm{act},l} = \frac{r_K}{\left[54k_l\ln^2(S_w)\right]^{1/3}} \approx \frac{r_K}{(54k_l)^{1/3}}s_w^{-2/3}. \tag{39}$$

Plume particles contribute to n_{wl} by

$$\varphi_l = \frac{1}{n_{wl}}\int_{r_{\mathrm{act},l}}^{\infty}\frac{\mathrm{d}n_{wl}}{\mathrm{d}r}\mathrm{d}r \simeq \frac{1}{1+(r_{\mathrm{act},l}/\bar{r}_l)^{\zeta_l}}, \tag{40}$$

$$\zeta_l = \frac{4}{\sqrt{2\pi}\ln\sigma_l}, \tag{41}$$

as derived in Appendix A; ζ_l is a size distribution slope parameter. Higher k_l values lead to smaller activation radii and hence increased fractions of activated particles. We note that the exact width of the gray transition zone in Figure 3 defining near-threshold contrails is affected by changes of the k value ascribed to the soot particles in soot-rich plumes. Increasing k_s by making the fuel more sulfur poor widens the transition zone, since higher supersaturations are needed to activate the same number of soot particles relative to more sulfur-rich conditions.

For later use, mean values of the slope parameter and threshold radius of activated droplet cores are defined by number-weighted averages over all plume particle types:

$$\zeta = \sum_l \varphi_l n_{wl}\zeta_l \Big/ \sum_l \varphi_l n_{wl} \text{ and} \tag{42}$$

$$r_{\mathrm{act}} = \sum_l \varphi_l n_{wl} r_{\mathrm{act},l} \Big/ \sum_l \varphi_l n_{wl}. \tag{43}$$

Combining equations (37)–(48) yields the number concentration of plume particles that activate into water droplets at a given supersaturation. The superscript (1) in equation (37) indicates that a second relationship, $n_w^{(2)}(s_w)$, is required to fix $n_\circ$, since the supersaturation where relaxation actually occurs is not yet known. This second relationship allows us to fix $s_{w\circ} = s_{mw}(T_\circ)$ along with $n_\circ = n_w^{(1)}(s_{w\circ}) = n_w^{(2)}(s_{w\circ})$ as the intersection between both expressions.

We obtain $n_w^{(2)}$ by evaluating the supersaturation equation

$$\frac{\mathrm{d}s_w}{\mathrm{d}t} = \mathcal{P}_w - \mathcal{L}_w \tag{44}$$

$$\mathcal{L}_w = \frac{4\pi}{\nu}\frac{1}{n_w^{\mathrm{sat}}}\int_{-\infty}^{t}\dot{n}_w\, r_w^2(t,t')\frac{\mathrm{d}r_w(t,t')}{\mathrm{d}t}\mathrm{d}t' \tag{45}$$

at the time $t = t_\circ$ where s_w starts to decline, i.e., when $\mathcal{P}_w = \mathcal{L}_w$. Here $\mathcal{P}_w$ is the net forcing of supersaturation (equation (6)) and $\mathcal{L}_w$ is the condensation sink. In equation (52), $\dot{n}_w(t,t')\mathrm{d}t'$ is the number of droplets at time t activated on contrail plume particles between t' and $t' + \mathrm{d}t'$, $r_w(t,t')$ is the mean radius at time t of water droplets which activated at $t' < t$, and $\mathrm{d}r_w(t,t')/\mathrm{d}t$ is the single droplet growth rate (equation (23)). Hence, $(4\pi r_w^2/\nu)\mathrm{d}r_w/\mathrm{d}t$ is the rate at which water molecules are transferred from the gas to the growing droplets. The lower integration limit has been extended to $-\infty$ under the assumption of a narrow activation pulse, approximated by an exponential, with characteristic time scale, τ_{act}:

$$\dot{n}_w(t,t') = \dot{n}_w(t)e^{-(t-t')/\tau_{\mathrm{act}}} \quad t' \le t. \tag{46}$$

The time t is later identified with the time of activation-relaxation, $t_\circ$. The activation time scale is chosen to match the time evolution of the activated droplet number prior to supersaturation relaxation:

$$\tau_{\mathrm{act}}^{-1} \equiv \frac{\partial\ln(n_w)}{\partial t} = \frac{\partial\ln(n_w)}{\partial s_w}\frac{\mathrm{d}s_w}{\mathrm{d}t}\Big|_{\mathcal{L}_w=0} \simeq \frac{2\zeta}{3s_w}\mathcal{P}_w, \tag{47}$$

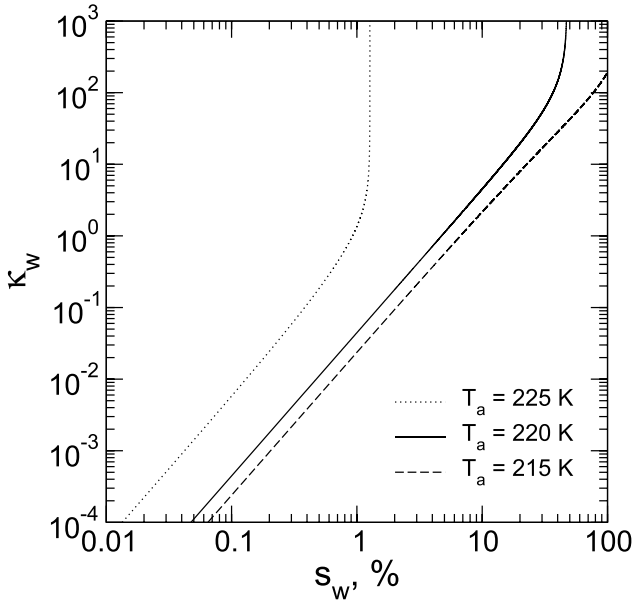

Figure 9. Activation-growth regime parameter versus supersaturation in plumes expanding at various ambient temperatures, evaluated along $s_w = s_{mw}(T)$ using typical values $r_{act} = 15$ nm and $\zeta = 2$.

(Appendix A). Together with the initial droplet growth time scale

$$\tau_{gw}^{-1} \equiv \frac{\partial \ln(r_w)}{\partial t}\Big|_{r_w=r_{act}} \simeq \frac{b_1}{r_{act}}, \tag{48}$$

with $b_1 = \nu v s_w n_w^{(sat)}/4$. We omit the term correcting τ_{gw} for diffusive uptake in the denominator of equation (48), since dry activation radii are typically smaller than 0.1 μm where these corrections are small.

We define the dynamical regime parameter

$$\kappa_w = \frac{\tau_{act}}{\tau_{gw}}, \tag{49}$$

characterizing slow ($\kappa_w \ll 1$) and fast ($\kappa_w \gg 1$) droplet growth regimes. In the fast growth regime, droplet sizes increase quickly during activation, while in the slow growth regime, all droplets activate before growth commences and droplets stay longer at sizes close to r_{act}.

We show $\kappa_w(s_w)$ in Figure 9 evaluated at $s_w = s_{mw}$ for different atmospheric temperatures. For entrained soluble particles already activating at $s_w < 1\%$, $\kappa_w \ll 1$ in all cases. This may no longer hold in near-threshold contrails (dotted curve) or for insoluble soot particles even in below-threshold contrails (solid and dashed curves), since most aircraft soot particles activate into droplets only at $s_w > 1\%$, in which case $\tau_{act} \propto s_w$ is longer and $\tau_{gw} \propto 1/s_w$ is shorter, so that $\kappa_w > 1$. The sharp increase of κ_w in the near-threshold case reflects the diminishing cooling rate (forcing) as $T \to T_a$. This increase also occurs in the below-threshold cases in the case of low droplet numbers, but at much higher supersaturation.

Since we cannot expect either growth regime to be exclusively realized (as after freezing-relaxation), we need to evaluate the supersaturation sink term equation (52) for all conceivable values of κ_w. We omit the diffusion correction in the growth law dr_w/dt, since final droplet sizes are unlikely to increase beyond a few 100nm (Figure 6). Carrying out the integration and defining $\mathcal{R}_w = \mathcal{L}_w/n_w$ as the supersaturation loss rate per droplet leads to

$$\mathcal{R}_w = \frac{b_1}{\nu} \frac{4\pi r_{act}^2}{n_w^{sat}} \left(1 + 2\kappa_w + 2\kappa_w^2\right). \tag{50}$$

Setting $\mathcal{P}_w = \mathcal{L}_w$ yields $n_w^{(2)}(s_w)$, the number concentration of droplets needed to cause supersaturation relaxation at a given value s_w:

$$n_w^{(2)} = \mathcal{P}_w/\mathcal{R}_w. \tag{51}$$

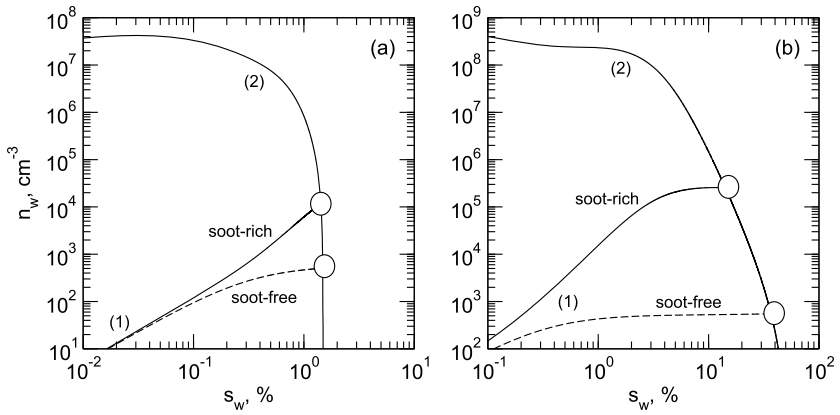

Figure 10. Droplet number concentrations versus plume supersaturation from the activation spectra of plume particles, $n_w^{(1)}$, and from the supersaturation relaxation requirement, $n_w^{(2)}$. We show (a) a near-threshold case and (b) a below-threshold case. The soot emission index is varied from soot rich (solid $n_w^{(1)}$ curves) to soot free (dashed $n_w^{(1)}$ curves) in both cases. In soot-free contrails, only entrained aerosol particles activate into water droplets. Activation-relaxation occurs at intersections between both curves and are indicated by open circles. Note the different scales in both panels.

In Figure 10, we illustrate both n_w solutions as a function of $s_w = s_{mw}$ for two atmospheric temperatures (a) near-threshold case and (b) below-threshold case. Activated nuclei numbers, $n_w^{(1)}$, are shown for soot-rich conditions (solid curve, $\mathrm{EI}_s = 10^{15}$ (kg-fuel)$^{-1}$) and without soot emissions, so that contrails only form on entrained particles (dashed curve, $n_a = 600$ cm^{-3}, $\mathrm{EI}_s = 0$). Those curves flatten as they approach the total local plume concentrations. Very few soot particles (but already a significant fraction of atmospheric particles) are activated below $s_w \approx 0.1$ % (Figure 10a), but the activated soot fraction continues to increase with s_w eventually dominating $n_w^{(1)}$. Droplet numbers required to quench s_w, $n_w^{(2)}$, are large falling off very rapidly as s_w approaches the point where the supersaturation forcing changes its sign ($s_w \approx 1$% in Figure 10a and $s_w \approx 50$% in Figure 10b).

Generally, at low s_w, high numbers $n_w^{(2)}$ are needed to deplete the supersaturation owing to the strong supersaturation forcing, but the number of plume particles $n_w^{(1)}$ that can actually be activated is still low. At high s_w, many particles can activate into droplets, and the number required to cause supersaturation relaxation is small due to the diminishing forcing. Circles in Figure 10 mark conditions at activation-relaxation fixing $n_\circ$ (and implicitly $T_\circ$, $s_{w\circ}$, and $t_\circ$). Removing soot emissions leads to fewer droplets regardless of T_a. The difference in $n_\circ$ between soot-rich and soot-free cases increases when contrails form in colder ambient air, where higher plume supersaturations are reached earlier in the plume and cooling rates are higher.

We also estimate the mean droplet radius, $r_\circ$, as an average over the activation pulse:

$$r_\circ = \frac{1}{n_\circ} \int_{-\infty}^{t_\circ} \dot{n}_w(t,t')\, r_w(t,t')\, \mathrm{d}t' = r_{\mathrm{act}}(1+\kappa_w)\,. \tag{52}$$

Contrail water droplets begin to freeze in the declining temperature with increasing probability. Activation-relaxation occurs close to freezing-relaxation, as explained above, especially near the formation threshold (Figures 3 and 8). We identify ice properties with the corresponding droplet particle properties taken at $t = t_\circ$ by setting $n_i = n_\circ$ and $r_i = r_\circ$. While the apparent ice emission index, AEI_i, inferred from equation (17) is independent of plume age, this may introduce a small error in the initial value of r_i, since ice particles continue to grow only for a very short time interval (between $t_\circ$ and $t_\star$). This error is probably within the uncertainty limits of our approach and diminishes further as the ice particles deposit more water vapor.

The nucleation burst scenario results in a unimodal population where most ice particles have similar sizes. In cases where droplets continue to be activated near freezing-relaxation, we still expect all droplets to freeze but their size distribution may be slightly broadened. Another factor affecting the ice particle size spectrum is turbulent plume mixing, as contrail particles in adjacent air parcels experience slightly different activation, freezing, and growth histories. It would be interesting to apply large-eddy simulations of the jet flow including contrail microphysics in order to elaborate the issue of spectral broadening.

We define a number of further ice variables useful for the interpretation of our results. The ratio of water-activated particles to all plume particles is given by

$$\Phi = \frac{n_\circ}{\sum_l n_{wl}} \tag{53}$$

and is equivalent to the fraction of frozen plume particles. The time invariant apparent emission index of ice particles follows from equation (17):

$$\mathrm{AEI}_i = \frac{\mathcal{N}_0}{\mathcal{D}} \frac{n_\circ}{\varrho}\,, \tag{54}$$

where ϱ and $\mathcal{D}$ are taken at $t_\circ$. The ice particles grow rapidly by vapor deposition from their approximate initial radius, $r_\circ$, as the plume air is highly supersaturated with respect to ice. The amount of water vapor between water and ice saturation available for ice growth is much larger than the ice water content at $t_\circ$. Ice particle mean radii, $r_i(t > t_\circ)$, may be estimated for short periods of time after formation from the droplet growth model, equations (32)–(34) applied to ice particle growth with initial conditions $r_i(t_\circ) = r_\circ$ and $S_i(t_\circ) = S_{w\circ} \cdot e_w(T_\circ)/e_i(T_\circ)$. In section 5, we discuss results from our model taken at the time of activation-relaxation, $t_\circ$; contrail properties at later stages of jet plume evolution, $t > t_\circ$, will be presented in future work.

The monodisperse contrail optical depth (OD) is calculated using the size-dependent scattering coefficient, $\mathcal{Q}$, from Mie theory, evaluated with a refractive index 1.33 at a wavelength of 0.55 µm [*Bohren and Huffman*, 2007]:

$$\mathrm{OD} \simeq \pi r_i^2 \mathcal{Q}(r_i) n_i d\,, \quad d = d_0/\sqrt{\mathcal{D}}\,, \tag{55}$$

disregarding the potential contribution of light absorption by soot inclusions in ice particles; d is the overall plume diameter. Light scattering probes the particle surface area, equation (55) provides us with lower limit OD values. In nature, ice particles will be size dispersed, which increases the mean particle surface area relative to the monodisperse approximation. It is not immediately obvious how slight deviations from the underlying assumptions in Mie theory of contrail ice particles being smooth, perfectly spherical scattering objects modifies OD predicted by equation (55). Finally, the imaginary part of the refractive index that controls the light absorption efficiency increases dramatically as soot volume fractions within ice particles increase [*Hong et al.*, 2008], causing a potentially higher extinction (scattering and absorption) efficiency of contrail ice particles in the early formation stage, depending on the physical mixing state of soot and ice components inside single contrail particles.

5. Results

5.1. Validation

We make a first attempt to check the agreement of our model results with in situ observations. To date, one observation has been documented [*Busen and Schumann*, 1995] providing all the information necessary to constrain our model. A drawback for validation is that this observation took place very close to the formation threshold temperature, where results are strongly affected by measurement uncertainties (Figure 2b). Furthermore, ice particle concentration and other variables needed to quantify contrail visibility close to the time of formation have not been measured. More recent contrail observations quantify the ice phase in contrails directly [*Voigt et al.*, 2011] but took place at subsaturated conditions in the vortex regime rendering a direct comparison with our results more difficult, since the jet wake structure becomes more inhomogeneous and ice particles may sublimate.

The contrail-producing research aircraft was the Deutsches Zentrum für Luft- und Raumfahrt (DLR) ATTAS equipped with Rolls-Royce/SNECMA M45H MK501 turbofan engines with core and bypass section [*Busen and Schumann*, 1995]. The jet engine diameter at the nozzle exit is $d_0 = 0.86$ m, the static core exhaust temperature is $T_0 = 563$ K, and the corresponding air density is $\varrho_0 = 0.19$ kgm^{-3}. The mixing factor at emission, $\mathcal{N}_0 = 64.6$ kg-air(kg-fuel)$^{-1}$, is computed from the core mass flow rate that includes air with which the fuel had been premixed upon combustion, $\dot{m}_0 = \varrho_0 A_0 u_0 = 8.2$ (kg-air)s^{-1} (axial exhaust velocity $u_0 = 350$ ms^{-1} in the core flow, core cross section $A_0 = 0.125$ m^2) and the fuel flow rate, $\dot{m}_f = 0.125$ (kg-fuel)s^{-1}. We estimate a mixing timescale $\tau_m = 5$ ms for a jet core radius $r_0 = 0.21$ m as used in equation (9). The engine diameter is $d_0 = 0.86$ m for use in equation (55). The soot number emission

Table 2. Model Sensitivity Studies, Ai–Av, of Contrail Observations Behind the DLR-ATTAS Aircraft in Different Meteorological Conditions[a]

	P (hPa)	RH (%)	RHI (%)	T_a (K)	$\Theta - T_a$ (K)	n_i (cm^{-3})	$t_\circ$ (s)	Φ (%)	r_i(μm)	OD
Ai	302.3	40.5	65	222.95	0.15	4.5×10^4	0.33	16	0.15	0.007
Aii	302.3	46.7	75	222.95	0.47	1.7×10^5	0.30	58	0.11	0.006
Aiii	302.3	40.3	65	222.45	0.64	2.3×10^5	0.28	72	0.10	0.007
Aiv	302.3	46.5	75	222.45	0.96	2.8×10^5	0.26	81	0.11	0.008
Av	287.4	45	73	220.7	2.1	3.8×10^5	0.21	93	0.11	0.014
B	250	60.8	100	220	4.6	1.2×10^5	0.34	92	0.20	0.13

[a]In Ai–Aiv, atmospheric temperature, T_a, and relative humidity, RH (over ice: RHI), are varied within experimental uncertainties relative to the near-threshold observation case [*Busen and Schumann*, 1995]. To analyze the observed below-threshold case Av [*Petzold et al.*, 1997], the same aircraft and emission parameters were used. Case B describes a baseline contrail. The difference between T_a and the formation threshold temperature, Θ, is indicated. Values of variables are taken at the time of activation-relaxation, $t_\circ$; total contrail particle number concentration, n_i; fraction of activated droplets (nuclei) or frozen fraction, Φ; initial mean particle radius, r_i; and solar contrail optical depth, OD, due to scattering of light at visible wavelengths.

index has been measured in flight, although during a different campaign [*Petzold et al.*, 1999b], yielding $EI_s = 1.7 \times 10^{15}$ (kg-fuel)$^{-1}$, $r_s = 17$ nm, and $\sigma_s = 1.55$. The σ_s value assumed here (1.7) is slightly larger than that inferred from the measurements to approximately account for a larger second size mode containing much fewer particles (less than 0.1% of the total particle number). We set $n_a = 0$ consistent with a previous study showing that visible contrail formation in this soot-rich case required a very high number of ice particles that could not be supplied by the atmosphere [*Kärcher et al.*, 1996]. As motivated in section 3, a reasonable choice of the effective solubility parameters for fresh soot particles is $k_s = 0.005$.

Observations were taken at $P = 302.3 \pm 0.7$ hPa, $T_a \simeq 223.45 \pm 0.5$ K, and for RH $\simeq$ 34–50 % (below ice saturation). The relative humidity estimates were based on radiosonde data taken at locations close to but outside the flight track. The short-lived contrail became clearly visible at an estimated plume age of 0.3s, about 35m behind the source aircraft [*Busen and Schumann*, 1995]. The water mass emission index and specific heat of fuel combustion were measured to be $\mathcal{M}_w = 1.21$ kg(kg-fuel)$^{-1}$ and $Q = 43.24$ MJ(kg-fuel)$^{-1}$, respectively; the overall propulsion efficiency was estimated to be $\eta = 0.14$, resulting in $G = 1.59$ PaK^{-1}.

Using the measured mean values for T_a and RH does not lead to contrail formation according to the thermodynamic theory. This could be caused by uncertainties in the determination of G or in measuring T_a and RH. To allow contrail formation, we reduce T_a and enhance RH within the measurement uncertainties. Since radiosonde data are known to have pronounced dry biases in upper tropospheric conditions, a 10% increase in RH from uncorrected radiosonde data is a conservative estimate. We further check whether the predicted solar optical depth of the observed contrail is large enough to explain its visibility. The optical depth should perhaps have been about 0.02 (a lower limit value for a distant observer) for this contrail. However, the exact optical depth threshold in this case is not known, since we can judge the visibility only by means of a photograph that was taken very closely behind the source aircraft. Therefore, OD thresholds applicable to this observation are probably smaller than 0.02.

Model results for this case are presented in Table 2 (cases Ai–Aiv), illustrating the sensitivity in contrail properties close to the formation threshold. As expected, a highly variable fraction, 16–93% of emitted soot particles, water-activates and freezes. All n_i values meet the visibility constraint, $n_i > 10^4$ cm^{-3}, inferred previously for the same observation (section 2.1). The computed times of contrail particle formation, ≈ 0.3 s, agree very well with the visual observation. The calculated (lower limit) optical depths, 0.007–0.014, might well suffice to explain contrail visibility. Given the uncertainties in calculating the total extinction (section 4.2.3), we do not explore the remaining discrepancy further but note that doubling k_s brings the estimated OD values into closer agreement without deteriorating the overall agreement. Although it is very likely that water supersaturation did occur in this case perhaps to a degree covered by cases Aiii and Aiv, it is possible that detailed simulations of the jet plume turbulence and dynamics might reveal even more favorable conditions for droplet activation and growth than estimated here.

The ATTAS performed several other contrail flights. One measurement was carried out at $P = 287.4$ hPa, $T_a = 220.7$ K, and RH $= 45$ % [*Petzold et al.*, 1997], producing contrails well below the formation threshold, so

that validation in this case is not hampered by the inherent uncertainty underlying cases Ai–Aiv. Ice particle numbers have been measured with an optical spectrometer probe and sizes have been determined using Mie theory. In the absence of more detailed information, we use the same aircraft/fuel/engine parameters for this case as well. Our model results are summarized in Table 2 (case Av). In addition, at $t = 1$ s, we compute $n_i = 9.4 \times 10^4$ cm^{-3} and $r_i = 0.4$ µm. At plumes ages < 2 s, about 750–1000cm^{-3} contrail ice particles have been measured across the young jet plume, with mean radii ≈ 0.45–1.35 µm.

Mean ice particle sizes from the model for the below-threshold case Av are at the low end of measured values and measured total numbers are substantially lower than predicted. This may be caused by missing coincidence corrections to the raw optical particle counter data. It is well known that cloud droplet probes and aerosol particle spectrometers can be subject to large, systematic coincidence errors [*Lance*, 2012]. Those measurement artifacts are instrument specific and can lead to very significant (at least fourfold) particle undercounting and oversizing (threefold to fivefold) biases.

It is not possible to determine in retrospect associated correction factors for the ATTAS case Av, some of which are presumably very substantial (A. Petzold, personal communication, 2014). There is no reason to expect new ice particle formation in the late jet or early vortex regime. Our bulk dilution model predicts a factor of about 5 decrease of n_i between plume ages 2s and 10s. The fact that n_i values measured at a plume age of 10s are higher than those measured below 2s [*Petzold et al.*, 1997, Table 5] thus lends support to the hypothesis of particle counting and sizing errors and demonstrates how challenging particle measurements in fresh contrails and comparisons with models are.

5.2. Discussion

We define a baseline case representing typical parameters of a large airliner cruising close to the extratropical tropopause in contrail-supporting (ice-supersaturated) atmospheric conditions. With this information, we analyze general features of the model solution and discuss the behavior of several contrail variables over a wide range of EI_s and T_a values. We recall that this discussion applies only to (desulfurized) fuel in which ultrafine volatile plume particles do not grow to sizes large enough to become activated into water droplets in below-threshold contrails at strongly reduced soot emissions in the presence of entrained ambient particles acting as condensation sinks.

For the soot-rich baseline contrail (case B in Table 2), we specify $T_0 = 600$ K, $\mathcal{N}_0^* = 60$, $\tau_m = 10$ ms, $d_0 = 2$ m, $k_s = 0.005$, $\sigma_s = 1.6$, $k_a = 0.5$, $\sigma_a = 2.2$, $r_s = 12.5$ nm, $r_a = 15$ nm, $EI_s = 5 \times 10^{14}$ (kg-fuel)$^{-1}$, $n_a = 600$ cm^{-3} ($\xi \simeq 150$), and $G = 1.64$ PaK^{-1}. In an ice-saturated atmosphere at $P = 250$ hPa and $T_a = 220$ K, this leads to a peak water saturation ratio in the plume without condensation of $S_\wedge = 1.45$ at $T_\wedge = 227.4$ K, first occurrence of water condensation at $T_\times = 238.8$ K, and an approximate threshold temperature $\Theta \simeq 224.6$ K. In case B, OD is much larger due mainly to a much larger jet engine diameter.

We have carried out a number of sensitivity studies for case B not included in Table 2. Decreasing the plume temperature at the engine exit (T_0) from 600K to 500K increases n_i by $\approx$ 3 %, while doubling the jet mixing time scale (τ_m) increases n_i more substantially (by $\approx$ 65 %). Increasing the plume mixing factor (β) from 0.9 to 1.5 results in a dramatic decrease in n_i by more than a factor of 10, but values of β as high as 1.5 might not be realistic. Doubling $\mathcal{N}_0^*$ reduces n_i by $\approx$ 50%. While those changes likely indicate correct tendencies, the estimated n_i changes are probably within the uncertainty of our idealized approach and are therefore not discussed any further. Changes in parameters modifying the mixing line slope (G), including $\mathcal{M}_w$, Q, and η, affect the formation threshold temperature as well as the peak value and production rate of supersaturation and may induce larger variations in contrail properties. We suggest to conduct systematic studies of their impact on n_i in future work and continue by exploring the general dependencies of important contrail variables at the time of activation-relaxation on particle emissions and on the state of the atmosphere.

Figure 11 presents our results for case B as a function of assumed soot particle number emission indices for different atmospheric temperatures. Clearly, EI_s is a key controlling factor of contrail particle formation, with apparent ice particle emission indices, AEI_i (Figure 11a), generally increasing with increasing EI_s with variable slopes. In the soot-rich regime, $AEI_i \approx EI_s$; for fixed EI_s, AEI_i increases rapidly with decreasing T_a in near-threshold contrails (dotted, dashed), while staying almost constant with decreasing T_a in below-threshold contrails (solid, dash-dotted). This is caused by the threshold behavior of plume particle activation (Figure 11b). In the soot-poor regime, AEI_i is limited by atmospheric particles and varies only slightly, because activation at various T_a occurs at different plume ages $t_\bullet$ (Figure 11c) at which point different amounts

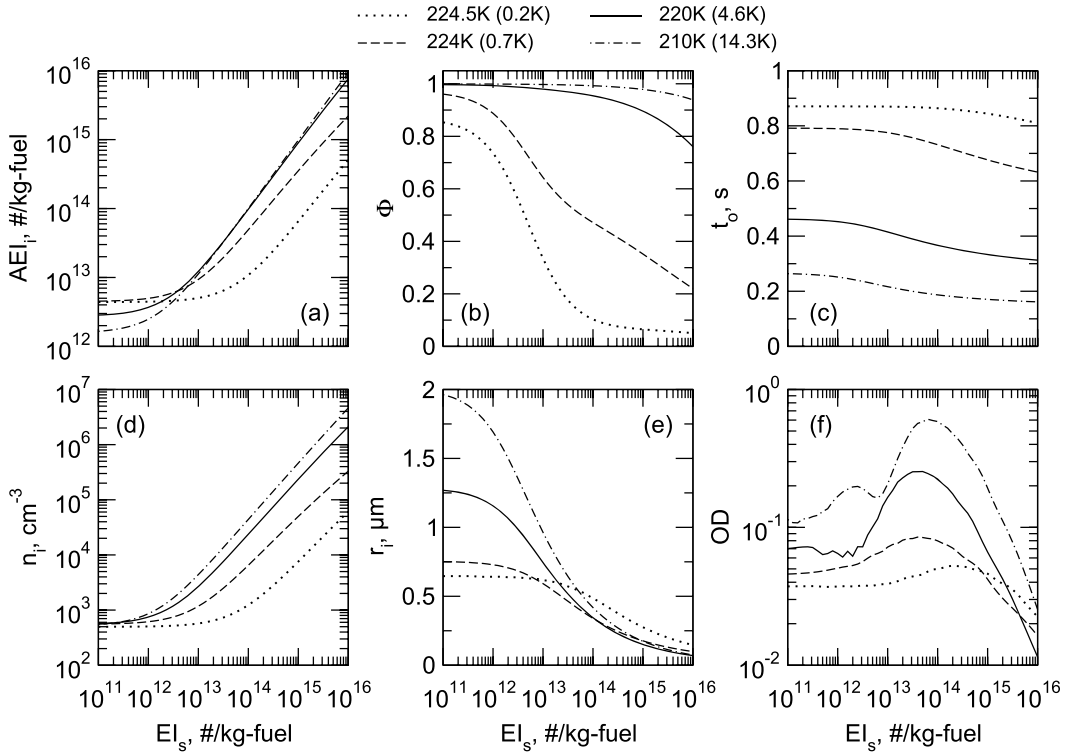

Figure 11. Model results versus soot number emission index for different atmospheric temperatures (difference between ambient temperature and formation temperature threshold) corresponding two near-threshold cases (dotted, dashed) and two below-threshold cases (solid, dash-dotted). Shown are results for the base case: (a) apparent ice particle number emission index, (b) fraction of water-activated and therefore frozen plume particles, and (c) time at activation-relaxation, and at the time of activation-relaxation: (d) total ice particle number concentration, (e) mean ice particle radius, and (f) shortwave optical depth.

of ambient particles have been entrained into the plume. The frozen plume particle fraction, Φ, remains small (< 0.1) close to the threshold in soot-rich fuel, as only very few soot particles can be activated into freezing water droplets at low supersaturations; Φ increases toward 0.8–0.9 in the soot-poor case, as the fully soluble atmospheric aerosols which take over the dominant part as contrail nuclei are more easily activated. If contrails form more than a few degrees of kelvin below the threshold, $\Phi \rightarrow 1$ in all cases. Activation-relaxation is completed earlier, i.e., at smaller values t_o (Figure 11c), the higher EI_s, since more droplets form at the same plume supersaturation. Contrail particle formation occurs in soot-rich cases typically at 0.2–0.4s, but considerably later in near-threshold contrails (0.6–0.9s).

Figure 11 shows (d) n_i, (e) r_i, and (f) OD, taken at $t = t_o$. We recall that we do not distinguish between activated (n_o) and frozen ($n_\star$) droplet number at this plume age, since we expect all droplets to freeze either around the same time or shortly thereafter. Ice particle number concentrations follow closely AEI_i, but exact values are time dependent due to plume dilution. Importantly, ice particle radii increase with decreasing EI_s and saturate at the lowest values in accordance with our analysis of droplet growth (Figure 6), revealing slow and fast condensation regimes with characteristic effects of T_a on r_i as explained below. Monodisperse optical depths vary with EI_s according to n_i and r_i, exhibiting Mie oscillations that would be smoothed out when averaged over an ice particle size distribution. The largest oscillation occurs when the mean ice particle diameter equals the wavelength (0.55 μm). Furthermore, OD values happen to maximize for soot emission levels $\approx 10^{14}$ (kg-fuel)$^{-1}$ and saturate as the exhaust becomes increasingly soot poor. Supplying very high soot emissions ($>10^{15}$ (kg-fuel)$^{-1}$) cause mean radii and therefore optical depths to decrease. Finally, OD tends to increase with decreasing T_a due mainly to increasing supersaturation and n_i values.

Figure 12 shows the same contrail variables as a function of assumed atmospheric temperature, T_a, expressed as an offset to the formation threshold temperature, $(\Theta - T_a)$, for various soot emission indices in the soot-poor (dotted), intermediate (dashed), and two soot-rich (solid, dash-dotted) regimes. The threshold behavior of

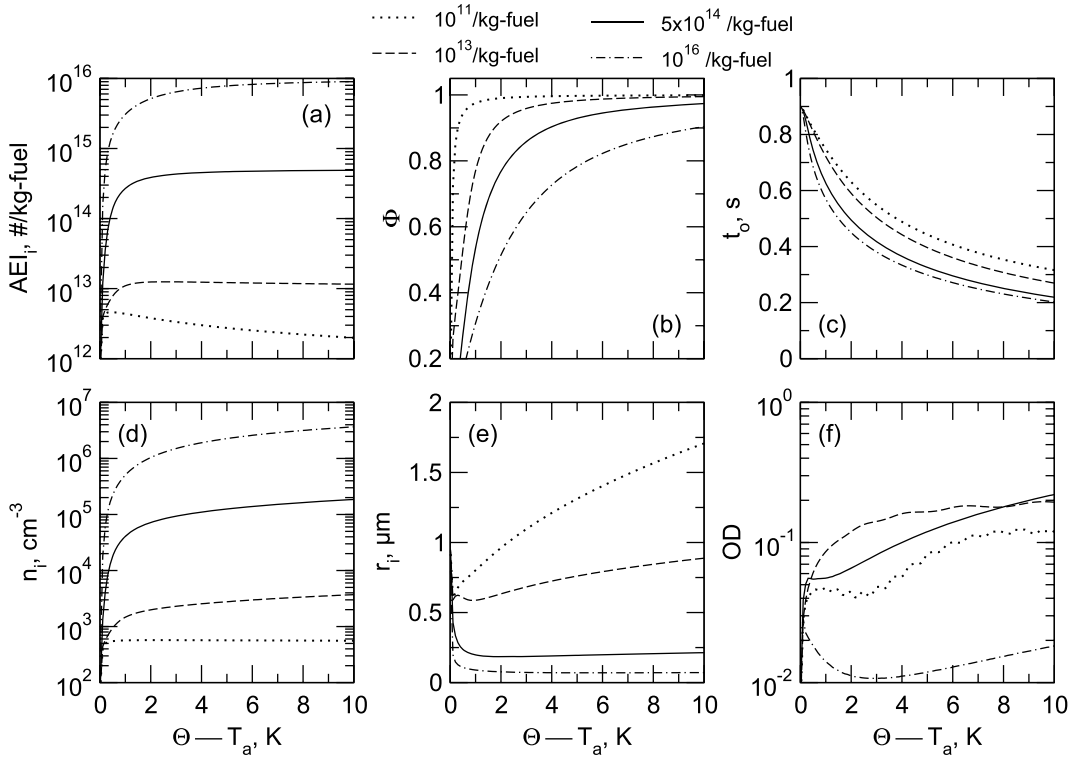

Figure 12. Model results as in Figure 11 but versus the offset between atmospheric temperature and threshold temperature ($\Theta \simeq 224.3-224.7$ K) for different soot emission indices corresponding to two soot-rich cases: $\xi = 2000-10,000$ (dash-dotted) and $\xi = 100-450$ (solid), one intermediate case: $\xi = 2-5$ (dashed), and one soot-poor case: $\xi \simeq 0.03$ (dotted). Shown are results for the base case: (a) apparent ice particle number emission index, (b) fraction of water-activated/frozen plume particles, and (c) time at activation-relaxation; and at the time of activation-relaxation: (d) total ice particle number concentration, (e) mean ice particle radius, and (f) shortwave optical depth.

droplet formation causes AEI_i and Φ to change very rapidly for $(\Theta - T_a) < 2$ K (Figures 12a and 12b). The exact behavior of AEI_i and Φ in near-threshold contrails depends on details of the soot activation spectrum, in particular on the choice of k_s, and on the slope of the mixing line. In soot-rich conditions, $AEI_i \rightarrow EI_s$ as T_a decreases, while in soot-poor conditions (blue curve) AEI_i slightly decreases, since activation-relaxation occurs at younger plume ages with correspondingly fewer entrained ambient particles. Figure 12c shows that colder contrails form earlier behind the source aircraft. Close to the threshold, t_o values tend to converge toward ≈ 0.9 s, independent of EI_s.

In soot-rich contrails, n_i (Figure 12d) continues to increase slightly as T_a decreases, as more (smaller) soot particles can be activated. Furthermore, r_i (Figure 12e) is mainly determined by the number of activated nuclei, as condensation is fast. Mean ice particle sizes are larger for low soot emissions (slow condensation) due to larger plume supersaturation. Contrail optical depths are larger in colder contrails but do not necessarily scale in proportion to T_a. As for the variations of OD with EI_s, this scaling behavior might average out once the monodisperse OD is integrated over a distribution of ice particle sizes.

The general trends of n_i with both EI_s and T_a discussed here agree qualitatively with numerical results [*Kärcher and Yu*, 2009], indicating that we have captured the principal physical processes determining contrail microphysical and optical properties at formation.

6. Conclusions

6.1. Summary

We have developed a minimal model to predict the formation and properties of water droplets and ice particles in jet aircraft contrails. The model is useful for studies in which soot emissions as well as engine parameters and ambient conditions need to be varied parametrically over a wide range of values. It provides

the conceptual framework and theoretical basis for further studies that address, e.g., mitigation of the contrail-induced climate impact. The model is based on the assumption that water saturation must be surpassed in aircraft exhaust plumes in order to produce visible contrails. The total number and mean size of nucleated ice particles and other contrail properties are computed for conditions in the jet regime. The time history of air parcels emanating from the center of the jet engine and the cooling rate required to generate supersaturation over supercooled water is constrained by jet plume dynamics and thermodynamics. Formation of contrail water droplets is caused by activation of, and uptake of water vapor on, plume particles serving as condensation nuclei. The droplets subsequently freeze homogeneously with immersed soot particles acting as passive cores. Freezing of water-activated plume particles tends to occur in a burst, implying that the vast majority of those droplets eventually freeze.

The underlying concept of activation-relaxation states that droplet nuclei are activated until the water droplet number is large enough to drive the supersaturation in the plume toward water saturation. This often occurs along with homogeneous droplet freezing. Eventually, freezing-relaxation drives the plume to ice saturation on a time scale determined by the total number and size of the nucleated ice particles.

The microphysics of contrail water droplet formation bears similarities with the suite of processes leading to the formation of natural clouds, major differences being the much more vigorous dynamical forcing in contrails leading to very short time scales of contrail particle formation and the ample supply of condensation nuclei leading to very small water droplets. For current jet fuels and engine technology, emitted soot particles play a decisive role in contrail formation, since they are, on the one hand, large enough to be activated into water droplets and, on the other hand, abundant to supersede the effect of particles entrained from the ambient air and to cause early visibility of contrails.

Variables necessary to initialize our model are the slope of the thermodynamic mixing line, air-to-fuel mass ratio and static exhaust gas temperature at jet engine core exit, and jet plume turbulent mixing time scale. The latter is estimated from the radius of the jet core and the corresponding axial flow velocity. The slope parameter taken from thermodynamic theory is fixed by air pressure, specific heat of fuel combustion, water vapor emission index, and overall propulsion efficiency. Furthermore, besides atmospheric temperature and relative humidity, total number, median size, and geometric standard deviation of lognormally distributed exhaust soot and atmospheric particle populations are required as input variables. Water condensation on plume particles is modeled by virtue of an effective solubility parameter depending on their actual chemical nature and mixing state.

We have introduced a number of regime parameters useful to categorize contrail particle formation conditions. For instance, for current soot-rich emission levels, water uptake on activated soot particles is fast relative to the time available for condensation and water droplets tend to freeze into a unimodal ice particle size distribution. The exact width and shape of the size spectrum is influenced by turbulent mixing and the moisture of the air entrained into the plume. Furthermore, we may generally distinguish between near-threshold and below-threshold contrails, as contrails forming close to the formation threshold temperature contain much fewer particles and are therefore optically thinner due to diminishing supersaturation inhibiting droplet and ice particle formation.

Our study confirms a significant dependence of contrail ice particle numbers and mean size on soot number emission indices and atmospheric temperature, a general trend seen in numerical simulations. Our model allows for conditions with (strongly) reduced soot particle emissions and is therefore ready for exploratory studies relating to effects on contrail properties of altered emissions or changing atmospheric conditions. Should the use of different fuels or combustion techniques change the water activation properties of soot particles, this could be taken into account by adjusting the associated solubility parameter in our model. We have made a first attempt to compare results with in situ observations. In view of experimental challenges to accurately quantify ice particle numbers and sizes in young contrails, considerably more effort is needed to carry out such comparisons. Future validation of the link between aircraft emissions and contrail ice particle properties might also require sophisticated computer models and dedicated airborne measurements of variables controlling droplet and ice formation in nascent contrails, including plume dilution factors and size-dependent water activation spectra of precursor particles. Along with insights gained from large-eddy simulations of turbulent jets, this may help assess our model's performance over a greater range of conditions.

While we consider the effect of atmospheric aerosol particles on ice formation—important for strongly reduced soot emissions—we opted to omit effects of ultrafine volatile plume particles, since water activation of those particles likely becomes important only for essentially soot-free aviation fuel producing large amounts of condensable material such as sulfuric acid and condensable organic vapors. For desulfurized aviation fuel, growth and water activation of ultrafine plume particles is limited by emissions of water-soluble organics. We suggest to characterize mass and solubility of organic emissions from alternative fuels in flight. Pure fuels with significant reductions in soot emissions (section 6.2) cannot be routinely used in order to meet engine certification requirements, but jet fuel can easily be desulfurized to minimize the impact of ultrafine plume particles on contrail ice formation.

When plotted against soot number emission indices in a double-logarithmic graph, apparent ice particle number emission indices exhibit a "hockey stick" pattern, in which the ice number is flat when limited by atmospheric particles in the soot-poor regime followed by a marked increase when the ice particle number increases in proportion to the number of emitted soot particles as the fuel becomes soot rich. Within 1–2K of the threshold formation temperature, ice particle numbers decline very strongly. The distinct threshold behavior and the width of the transition zone—measured by the temperature offset between the environment and the formation threshold—is affected by details of the activation spectrum of plume particles and the slope of the mixing line.

As aircraft soot emissions are engine and fuel dependent and also vary with the speed of the aircraft (hence, with the meteorological situation), we expect initial contrail variables to vary with the meteorological situation. Also, in the absence of soot emissions, we expect a wide range of contrail properties depending on the number of atmospheric aerosol particles. Free tropospheric aerosol number concentrations tend to be higher in summer than in winter and vary considerably regionally depending on proximity to aerosol source regions and processing within clouds. The fraction of water-activated and therefore frozen plume particles is close to unity at typical temperatures prevailing at cruise altitudes (near or below 220K), but frozen fractions stay lower closer to formation threshold temperatures (220–225K). For current soot emissions, contrails become visible for distant observers typically at plume ages $\approx$ 0.3 s and contain numerous ice particles with mean radii of several 100nm at formation. The time of formation and the mean size can increase substantially when ambient particles serve mainly as droplet nuclei. In either case, mean size, water content, and optical depth of ice particles increase very rapidly in the jet plume as they remove the high supersaturation over ice prevailing at their formation. Contrail optical depths at formation depend strongly on atmospheric temperature and on soot emissions.

In future work, we may capitalize on this model development by expanding our concept to cover physical processes changing contrail ice particle properties in the vortex regime. In this regard, it would be interesting to study how much the atmosphere must be ice supersaturated in order to stabilize fresh contrail ice particles against sublimation in sinking (warming) aircraft wake vortices. With such an extension, our model may form the basis of a parameterization scheme for use in global models that can be employed to determine the relative impact of atmospheric conditions and aircraft/fuel/engine-related parameters on the climate impact of contrail cirrus.

Furthermore, using numerical models to simulate the microphysical pathway to contrail formation, links can be studied in greater detail between plume dynamics, condensable vapors, and water condensation nuclei activity of plume particles prior to contrail formation. We encourage comparisons of results from process models with in situ measurements in future collaborative efforts, understanding that such comparisons will be frustrated by difficulties to accurately determine plume dilution factors and particle numbers due to the large internal variability in plume processes and due to instrumental limitations. Another difficulty arises from the fact that our bulk model does not capture the large degree of variability in particle properties in contrailing jet plumes. This variability arises from different dynamical and microphysical histories of air parcels emanating from jet engines at different locations and could be further explored using large-eddy simulations of turbulent jet plumes coupled to simplified ice microphysical schemes.

6.2. Implications for Effects of Alternative Aviation Fuels

The use of advanced alternative fuels in aviation offers one possibility to mitigate the contrail cirrus climate impact by causing reduced soot particle emissions by number and mass. The chemical composition of alternative aviation fuels can be significantly different from conventional jet fuel, containing significantly reduced aromatic (and therefore soot) and sulfur concentrations relative to kerosene. Blending such fuels

with kerosene in order to meet certification requirements leads to smaller soot reductions, so that contrail formation likely continues to take place in the soot-rich regime. We base this conjecture on ground-based measurements of aircraft engine emissions indicating large reductions of nonvolatile particle emissions at engine power settings corresponding to cruise conditions when using synthetic (e.g., Fischer-Tropsch) fuels [*Beyersdorf et al.*, 2014]. However, extrapolation of these results to conditions at cruise is uncertain.

A recent study highlights the difficulty in estimating aircraft soot emission indices without guidance by in-flight measurements and suggests that global civil aviation soot mass emissions have been underestimated [*Stettler et al.*, 2013]. Due to the lack of properly evaluated mass-size relationships for aviation soot, it is not known how much number emission indices are affected. The strong impact of soot emissions in determining contrail ice particle properties and the large mitigation potential underscores the need for much better predictions of soot emissions at cruise than currently available, inasmuch as there are no plans to measure soot number emission indices from all existing aircraft engines.

It may be technically feasible to design desulfurized, essentially soot-free aviation fuels as alternatives to kerosene, so that contrail formation would take place mainly on atmospheric particles in the intermediate or soot-poor regime. For such fuels, it should be studied whether remaining unburnt hydrocarbons were capable of producing enough ultrafine volatile plume particles contributing to ice formation in low-temperature contrails by growing chemi-ion produced particles to sufficiently large sizes. Our model may be extended to include these effects, but detailed numerical simulations and targeted exhaust plume measurements are necessary to better understand the underlying physical processes leading to contrail droplet activation from nanometer-sized precursor particles.

Appendix A: Time Scale of Plume Particle Activation

The rate of droplet nuclei activation is given by

$$\tau_{\mathrm{act}}^{-1} = \frac{\partial \ln(n_w)}{\partial s_w} \mathcal{P}_w \,. \tag{A1}$$

The supersaturation nuclei spectrum gives the cumulative number concentration of aerosol particles activated into water droplets above a given supersaturation,

$$\frac{\partial \ln(n_w)}{\partial s_w} = \frac{\partial \ln(n_w)}{\partial r} \frac{\mathrm{d}r}{\mathrm{d}s_w} \,, \tag{A2}$$

where $r = r_{\mathrm{act}}(s_w)$ denotes the dry radius of plume particles activating at s_w.

The first term follows from equation (22) as an integral over a single lognormal particle size distribution:

$$\varphi = \frac{1}{2}[1 - \mathrm{erf}(z)] \,, \quad z = \frac{\ln(r/\bar{r})}{\sqrt{2}\ln\sigma} \,. \tag{A3}$$

The error function, erf(z), is approximated by $\tanh(2z/\sqrt{\pi})$ leading to the cumulative fraction of activated particles

$$\varphi \simeq \frac{1}{1 + (r/\bar{r})^{\zeta}} \overset{r \gg \bar{r}}{\longrightarrow} \left(\frac{\bar{r}}{r}\right)^{\zeta} \,, \quad \zeta = \frac{4}{\sqrt{2\pi}\ln\sigma} \tag{A4}$$

(the limit is taken to represent the large-size tail of the distribution); hence, $\varphi \propto n_w \propto r^{-\zeta}$:

$$\frac{\partial \ln(n_w)}{\partial r} = -\frac{\zeta}{r} \,. \tag{A5}$$

The tail of a lognormal distribution has a variable slope; hence, the true slope is smaller than ζ as $r \to \bar{r}$. The second term in equation (A2) follows from equation (39)

$$\frac{\mathrm{d}r}{\mathrm{d}s_w} = -\frac{2}{3}\frac{r}{s_w} \,. \tag{A6}$$

Together, equations (A5) and (A6) lead to the activation spectrum, $\partial \ln(n_w)/\partial \ln(s_w) = 2\zeta/3$, and to τ_{act} (equation (47)). Generalization to multiple particle size modes is straightforward by using number-weighted averages for ζ and r_{act} according to equations (49) and (50).

Notation

AEI, EI	(Apparent) number emission index.
FSC	Fuel sulfur (S) content.
IWC	Ice water content.
LWV	Liquid water volume.
OD	Shortwave optical depth.
RH, RHI	Atmospheric relative humidity, over ice.
a	Atmospheric conditions.
c	Droplet core particles.
f	Aviation jet fuel.
g	Ice particle growth.
i	Ice particles, ice phase.
l	Plume particle type (s, a).
m	Jet plume mixing.
s	Aircraft soot particles.
w	Water droplets, liquid water phase.
0	Jet exit plane (initial).
act, frz	Plume particle activation, droplet freezing.
$\times$	Plume conditions at first water saturation.
$\circ$	Conditions at activation-relaxation.
$\star$	Conditions at freezing-relaxation.
$\wedge$	Maximum value in plume conditions.
A	Jet plume cross section.
α	Mass accommodation coefficient.
β	Plume dilution parameter.
a_1, a_2	Parameters in freezing rate coefficient.
b_1, b_2	Parameters in particle growth equation.
c_p	Isobaric specific heat of air.
d, d_0	Jet plume (engine) diameter.
D	Molecular diffusion coefficient of water vapor in air.
$\mathcal{D}$	Jet plume dilution factor.
ϵ	Scaled turbulent diffusivity.
G	Slope of average plume mixing line.
j	Plume particle activation pulse.
$\mathcal{J}$	Flux of molecules in air.
J	Homogeneous freezing rate coefficient.
k	Effective solubility parameter.
k_B	Boltzmann's constant.
κ	Activation- (freezing-) relaxation parameter.
λ	Freezing regime parameter.
$\mathcal{L}$	Water supersaturation loss rate.
$\dot{m}$	Mass flow rate.
$\mathcal{M}$	Mass emission index.
$n, \dot{n}$	Number concentration, contrail particle formation rate.
η	Overall aircraft propulsion efficiency.
$\mathcal{N}$	Mass-based plume mixing factor.
ω	Jet plume mixing rate.
p, P	Vapor partial pressure, air pressure.
φ	Cumulative number fraction of water-activated plume particles.
Φ	Total number fraction of water-activated (frozen) plume particles.
ψ	Water condensation regime parameter.
$\mathcal{P}$	Water supersaturation production rate.
Q	Specific heat of fuel combustion.
$\mathcal{Q}$	Mie scattering coefficient.

ϱ	Particle mass density.
r	Particle radius.
$\mathcal{R}$	Water supersaturation loss rate per droplet, $\mathcal{R} = \mathcal{L}/n_w$.
s	Supersaturation, $s = S - 1$.
S	Saturation ratio.
t	Jet plume age ($t = 0$ at jet engine exit plane).
τ	Characteristic timescale.
T	Jet plume temperature.
$\dot{T}$	Jet plume cooling rate.
Θ (Θ_G)	Contrail formation threshold temperature (at RH = 100%).
u	Axial jet velocity.
v	Molecular thermal speed.
ν	Molecular volume in a particle.
x	Axial distance from jet (nozzle) exit plane.
ξ	Contrail regime parameter.
ζ	Particle size distribution slope parameter.

Acknowledgments

This work was performed within the project "Emissions and Climate Impact of Alternative Fuel" (ECLIF) funded by DLRs aviation programme. One of us (B.K.) is grateful for fruitful discussions with Patrick LeClerq (DLR Institute of Combustion Technology) on the prospect of designing synthetic aviation fuels, with Bruce Anderson (NASA Langley), Richard Moore (NASA Langley), Andreas Petzold (Research Center Jülich), Tina Jurkat (DLR IPA), Christiane Voigt (DLR IPA), and Bernadett Weinzierl (DLR IPA) on in situ measurements in aircraft exhaust plumes and contrails, and with Roberto Paoli (CERFACS Toulouse), Richard Miake-Lye (Aerodyne Research), and Fangqun Yu (State University of New York at Albany) on numerical simulations of contrail particle formation and jet plume dynamics. All data used in this paper are available in *Busen and Schumann* [1995], *Petzold et al.* [1997], and *Petzold et al.* [1999b] cited in the reference list.

References

Abramovitch, G. N. (1963), *The Theory of Turbulent Jets*, MIT Press, Cambridge, Mass.

Anderson, B. E., et al. (2011), Alternative aviation fuel experiment (AAFEX), *Tech. Memo., NASA/TM-2011-217059*, Nat. Aeronaut. and Space Adm., Langley Research Center, Hampton.

Appleman, H. (1953), The formation of exhaust condensation trails by jet aircraft, *Bull. Am. Meteorol. Soc.*, *34*, 14–20.

Beyersdorf, A. J., et al. (2014), Reductions in aircraft particulate emissions due to the use of Fischer-Tropsch fuels, *Atmos. Chem. Phys.*, *14*, 11–23.

Bockhorn, H. (1994), *Soot Formation in Combustion, Mech. and Models*, Springer, Berlin.

Bohren, C. F., and D. R. Huffman (2007), *Absorption and Scattering of Light by Small Particles*, Wiley, New York.

Bond, T. C., et al. (2013), Bounding the role of black carbon in the climate system—A scientific assessment, *J. Geophys. Res. Atmos.*, *118*, 5380–5552, doi:10.1002/jgrd.50171.

Brock, C. A., F. P. Schröder, B. Kärcher, A. Petzold, R. Busen, M. Fiebig, and J. C. Wilson (2000), Ultrafine particle size distributions measured in aircraft exhaust plumes, *J. Geophys. Res.*, *105*, 26,555–26,568.

Brown, R. C., R. C. Miake-Lye, M. R. Anderson, and C. E. Kolb (1997), Aircraft sulfur emissions and the formation of visible contrails, *Geophys. Res. Lett.*, *24*, 385–388.

Burkhardt, U., and B. Kärcher (2009), Process-based simulation of contrail cirrus in a global climate model, *J. Geophys. Res.*, *114*, D16201, doi:10.1029/2008JD011491.

Burkhardt, U., and B. Kärcher (2011), Global radiative forcing from contrail cirrus, *Nat. Clim. Change*, *1*, 54–58.

Burkhardt, U., B. Kärcher, M. Ponater, K. Gierens, and A. Gettelman (2008), Contrail cirrus supporting areas in model and observations, *Geophys. Res. Lett.*, *35*, L16808, doi:10.1029/2008GL034056.

Busen, R., and U. Schumann (1995), Visible contrail formation from fuels with different sulfur contents, *Geophys. Res. Lett.*, *22*, 1357–1360.

Döpelheuer, A. (2002), Anwendungsorientierte Verfahren zur Bestimmung von CO, HC und Russ aus Luftfahrttriebwerken [in German], PhD dissertation, DLR Institute for Propulsion Technology, Cologne, Germany.

Ford, I. J. (1998), Ice nucleation in jet aircraft exhaust plumes, in *Air Pollution Research Report 68: Pollution From Aircraft Emissions in the North Atlantic Flight Corridor (POLINAT 2), Report EUR 18877*, edited by U. Schumann, pp. 269–287, European Commission DG, Brussels, Belgium.

Gettelman, A., E. J. Fetzer, A. Eldering, and F. W. Irion (2006), The global distribution of supersaturation in the upper troposphere from the atmospheric infrared sounder, *J. Clim.*, *19*, 6089–6103.

Gierens, K., and U. Schumann (1996), Colors of contrails from fuels with different sulfur contents, *J. Geophys. Res.*, *101*, 16,731–16,736.

Heymsfield, A., D. Baumgardner, P. DeMott, P. Forster, K. Gierens, and B. Kärcher (2010), Contrail microphysics, *Bull. Am. Meteorol. Soc.*, *91*, 465–472.

Heymsfield, A. J., G. Thompson, H. Morrison, A. Bansemer, R. M. Rasmussen, P. Minnis, Z. Wang, and D. Zhang (2011), Formation and spread of aircraft-induced holes in clouds, *Science*, *333*, 77–81.

Holzäpfel, F. (2003), Probabilistic two-phase wake vortex decay and transport model, *J. Aircr.*, *40*, 323–331.

Hong, G., Q. Feng, P. Yang, G. W. Kattawar, P. Minnis, and Y. Hu (2008), Optical properties of ice particles in young contrails, *J. Quant. Spectrosc. Radiat. Transfer*, *109*, 2635–2647.

Iwabuchi, H., P. Yang, K. N. Liou, and P. Minnis (2012), Physical and optical properties of persistent contrails: Climatology and interpretation, *J. Geophys. Res.*, *117*, D06215, doi:10.1029/2011JD017020.

Jensen, E. J., O. B. Toon, R. F. Pueschel, J. Goodman, G. W. Sachse, B. E. Anderson, K. R. Chan, D. Baumgardner, and R. C. Miake-Lye (1998), Ice crystal nucleation and growth in contrails forming at low ambient temperatures, *Geophys. Res. Lett.*, *25*, 1371–1374.

Kärcher, B. (1994), Transport of exhaust products in the near trail of a jet engine under atmospheric conditions, *J. Geophys. Res.*, *99*, 14,509–14,517.

Kärcher, B. (1998a), Physicochemistry of aircraft-generated liquid aerosols, soot, and ice particles: 1. Model description, *J. Geophys. Res.*, *103*, 17,111–17,128.

Kärcher, B. (1998b), On the potential importance of sulfur-induced activation of soot particles in nascent jet aircraft exhaust plumes, *Atmos. Res.*, *146*, 293–305.

Kärcher, B. (1999), Aviation-produced aerosols and contrails, *Surv. Geophys.*, *20*, 113–167.

Kärcher, B., and P. Fabian (1994), Dynamics of aircraft exhaust plumes in the jet regime, *Ann. Geophys.*, *12*, 911–919.

Kärcher, B., and F. Yu (2009), Role of aircraft soot emissions in contrail formation, *Geophys. Res. Lett.*, *36*, L01804, doi:10.1029/2008GL036649.

Kärcher, B., T. Peter, and R. Ottmann (1995), Contrail formation: Homogeneous nucleation of H_2SO_4/H_2O droplets, *Geophys. Res. Lett.*, *22*, 1501–1504.
Kärcher, B., T. Peter, U. Biermann, and U. Schumann (1996), The initial composition of jet condensation trails, *J. Atmos. Sci.*, *53*, 3066–3083.
Kärcher, B., R. Busen, A. Petzold, F. P. Schröder, U. Schumann, and E. J. Jensen (1998), Physicochemistry of aircraft generated liquid aerosols, soot, and ice particles: 2. Comparison with observations and sensitivity studies, *J. Geophys. Res.*, *103*, 17,129–17,148.
Kärcher, B., R. P. Turco, F. Yu, M. Y. Danilin, D. K. Weisenstein, and R. Busen (2000), A unified model for ultrafine aircraft particle emissions, *J. Geophys. Res.*, *105*, 29,379–29,386.
Kärcher, B., O. Möhler, P. J. DeMott, S. Pechtl, and F. Yu (2007), Insights into the role of soot aerosols in cirrus cloud formation, *Atmos. Chem. Phys.*, *7*, 4203–4227.
Kärcher, B., B. Mayer, K. Gierens, U. Burkhardt, H. Mannstein, and R. Chatterjee (2009), Aerodynamic contrails: Microphysics and optical properties, *J. Atmos. Sci.*, *66*, 227–243.
Koehler, K. A., P. J. DeMott, S. M. Kreidenweis, O. R. Popovicheva, M. D. Petters, C. M. Carrico, E. D. Kireeva, T. D. Khokhlova, and N. K. Shonija (2009), Cloud condensation nuclei and ice nucleation activity of hydrophobic and hydrophilic soot particles, *Phys. Chem. Chem. Phys.*, *36*, 7741–8104.
Kreidenweis, S. M., M. D. Petters, and P. Y. Chuang (2009), Cloud particle precursors, in *Clouds in the Perturbed Climate System: Their Relationship to Energy Balance, Atmospheric Dynamics, and Precipitation, Strüngmann Forum Report*, vol. 2, edited by J. Heintzenberg and R. J. Charlson, pp. 291–317, MIT Press, Cambridge, Mass.
Lamquin, N., C. J. Stubenrauch, K. Gierens, U. Burkhardt, and H. Smit (2012), A global climatology of upper tropospheric ice supersaturation occurrence inferred from the Atmospheric Infrared Sounder calibrated by MOZAIC, *Atmos. Chem. Phys.*, *12*, 381–405.
Lance, S. (2012), Coincidence errors in a cloud droplet probe (CDP) and a cloud and aerosol spectrometer (CAS), and the improved performance of a modified CDP, *J. Atmos. Oceanic Technol.*, *29*, 1532–1541.
Lewellen, D. C., and W. S. Lewellen (2001), The effects of aircraft wake dynamics on contrail development, *J. Atmos. Sci.*, *58*, 390–406.
Miake-Lye, R. C., M. Martinez-Sanchez, R. C. Brown, and C. E. Kolb (1993), Plume and wake dynamics, mixing and chemistry behind an HSCT aircraft, *J. Aircr.*, *30*, 467–479.
Murphy, D. M., and T. Koop (2005), Review of the vapour pressures of ice and supercooled water for atmospheric applications, *Q. J. R. Meteorol. Soc.*, *131*, 1539–1565.
Murphy, D. M., D. S. Thomson, and M. J. Mahoney (1998), In situ measurements of organics, meteoritic material, mercury, and other elements at 5 to 19 kilometers, *Science*, *282*, 1664–1669.
Paoli, R., J. Hélie, and T. Poinsot (2004), Contrail formation in aircraft wakes, *J. Fluid Mech.*, *502*, 361–373.
Paoli, R., L. Nybelen, J. Picot, and D. Cariolle (2013), Effects of jet/vortex interaction on contrail formation in supersaturated conditions, *Phys. Fluids*, *25*, 053305, doi:10.1063/1.4807063.
Papamoschou, D., and A. Roshak (1988), The compressible turbulent shear layer: An experimental study, *J. Fluid Mech.*, *197*, 453–477.
Paugam, R., R. Paoli, and D. Cariolle (2010), Influence of vortex dynamics and atmospheric turbulence on the early evolution of a contrail, *Atmos. Chem. Phys.*, *10*, 3933–3952.
Petters, M. D., and S. M. Kreidenweis (2007), A single parameter representation of hygroscopic growth and cloud condensation nucleus activity, *Atmos. Chem. Phys.*, *7*, 196–1971.
Petzold, A., and F. P. Schröder (1998), Jet engine exhaust aerosol characterization, *Aerosol Sci. Technol.*, *28*, 62–76.
Petzold, A., et al. (1997), Near-field measurements on contrail properties from fuels with different sulfur content, *J. Geophys. Res.*, *102*, 29,867–29,880.
Petzold, A., J. Ström, S. Ohlsson, and F. P. Schröder (1998), Elemental composition and morphology of ice-crystal residual particles in cirrus clouds and contrails, *Atmos. Res.*, *49*, 21–34.
Petzold, A., A. Döpelheuer, C. A. Brock, and F. P. Schröder (1999a), In situ observations and model calculations of black carbon emission by aircraft at cruise altitude, *J. Geophys. Res.*, *104*, 22,171–22,181.
Petzold, A., J. Ström, F. P. Schröder, and B. Kärcher (1999b), Carbonaceous aerosol in jet engine exhaust: Characteristics and implications for heterogeneous chemical reactions, *Atmos. Environ.*, *33*, 2689–2698.
Petzold, A., M. Gysel, X. Vancassel, R. Hitzenberger, H. Puxbaum, S. Vrochticky, E. Weingartner, U. Baltensperger, and P. Mirabel (2005), On the effects of organic matter and sulphur-containing compounds on the CCN activation of combustion particles, *Atmos. Chem. Phys.*, *5*, 3187–3203.
Ponater, M., S. Marquart, and R. Sausen (2002), Contrails in a comprehensive global climate model: Parameterization and radiative forcing results, *J. Geophys. Res.*, *107*(D13), 4164, doi:10.1029/2001JD000429.
Popovicheva, O. B., N. M. Persiantseva, E. E. Lukhovitskaya, N. K. Shonija, N. A. Zubareva, B. Demirdjian, D. Ferry, and J. Suzanne (2004), Aircraft engine soot as contrail nuclei, *Geophys. Res. Lett.*, *31*, L11104, doi:10.1029/2003GL018888.
Pruppacher, H. R., and J. D. Klett (1997), *Microphysics of Clouds and Precipitation*, Kluwer Acad., Dordrecht.
Riechers, B., F. Wittbracht, A. Hütten, and T. Koop (2013), The homogeneous ice nucleation rate of water droplets produced in a microfluidic device and the role of temperature uncertainty, *Phys. Chem. Chem. Phys.*, *15*, 5873–5887.
Rojo, C., X. Vancassel, P. Mirabel, J.-L. Ponche, and F. Garnier (2015), Impact of alternative jet fuels on aircraft-induced aerosols, *Fuel*, *144*, 335–341.
Schmidt, E. (1941), Die Entstehung von Eisnebel aus den Auspuffgasen von Flugmotoren, in *Schriften der Deutschen Akademie für Luftfahrtforschung*, vol. 44, pp. 115, Verlag R. Oldenbourg, Münich and Berlin, Germany.
Schröder, F. P., B. Kärcher, A. Petzold, R. Baumann, R. Busen, C. Hoell, and U. Schumann (1998), Ultrafine aerosol particles in aircraft plumes: In situ observations, *Geophys. Res. Lett.*, *25*, 2789–2792.
Schröder, F. P., B. Kärcher, C. Duroure, J. Ström, A. Petzold, J.-F. Gayet, B. Strauss, P. Wendling, and S. Borrmann (2000), On the transition of contrails into cirrus clouds, *J. Atmos. Sci.*, *57*, 464–480.
Schröder, F. P., B. Kärcher, M. Fiebig, and A. Petzold (2002), Aerosol states in the free troposphere at northern midlatitudes, *J. Geophys. Res.*, *107*(D21), 8126, doi:10.1029/2000JD000194.
Schumann, U. (1996), On conditions for contrail formation from aircraft exhausts, *Meteorol. Z.*, *5*, 4–23.
Stettler, M. E. J., A. M. Boies, A. Petzold, and S. R. H. Barrett (2013), Global civil aviation black carbon emissions, *Environ. Sci. Technol.*, *47*, 10,397–10,404.
Tollmien, W. (1926), Berechnung turbulenter Ausbreitungsvorgänge, *Z. Angew. Math. Mech.*, *6*, 468–478.
Twohy, C. H., and B. W. Gandrud (1998), Electron microscope analysis of residual particles from aircraft contrails, *Geophys. Res. Lett.*, *25*, 1359–1362.
Twomey, S. (1977), *Atmospheric Aerosols, Dev. in Atmos. Sci.*, vol. 7, Elsevier, Amsterdam.

Unterstrasser, S., and I. Sölch (2010), Study of contrail microphysics in the vortex phase with a Lagrangian particle tracking model, *Atmos. Chem. Phys.*, *10*, 10,003–10,015.

Voigt, C., U. Schumann, P. Jessberger, T. Jurkat, A. Petzold, J.-F. Gayet, M. Krämer, T. Thornberry, and D. W. Fahey (2011), Extinction and optical depth of contrails, *Geophys. Res. Lett.*, *38*, L10807, doi:10.1029/2011GL046884.

Wong, H.-W., and R. C. Miake-Lye (2010), Parametric studies of contrail ice particle formation in jet regime using microphysical parcel modeling, *Atmos. Chem. Phys.*, *10*, 3261–3272.

Wong, H.-W., et al. (2013), Laboratory and modeling studies on the effects of water and soot emissions and ambient conditions on the properties of contrail ice particles in the jet regime, *Atmos. Chem. Phys.*, *13*, 10,049–10,060.

Yu, F., and R. P. Turco (1997), The role of ions in the formation and evolution of particles in aircraft plumes, *Geophys. Res. Lett.*, *24*, 1927–1930.

Yu, F., and R. P. Turco (1998), Contrail formation and impacts on aerosol properties in aircraft plumes: Effects of fuel sulfur content, *Geophys. Res. Lett.*, *25*, 313–316.

Yu, F., R. P. Turco, and B. Kärcher (1999), The possible role of organics in the formation and evolution of ultrafine aircraft particles, *J. Geophys. Res.*, *104*, 4079–4087.